IRA Technical Report

Medicina Array Demonstrator:

Overview and Results of the third campaign

VERSION 1.0

G. Pupillo[1], G. Naldi[1], A. Mattana[1], J. Monari[1], M. Poloni[1], F. Perini[1], M. Schiaffino[1], G. Bianchi[1], P. Bolli[2], A. Lingua[3], I. Aicardi[3], H. Bendea[3], P. Maschio[3], M. Piras[3], G. Virone[4], F. Paonessa[4], Z. Farooqui[4], R. Tascone[4], A. Tibaldi[4]

Referee: M. Bartolini[1]

IRA 482/14

(1) Istituto di Radioastronomia di Bologna – INAF
(2) Osservatorio Astrofisico di Arcetri - INAF
(3) DIATI - Politecnico di Torino
(4) IEIIT - CNR di Torino

Index

1. Introduction

This document describes the activity performed during the third measurement session of the Medicina Array Demonstrator, hereafter called MAD-3.

MAD-3 mainly consists in a small low-frequency array implementing, on a small-scale, a similar structure of the SKA-LFAA element (Square Kilometer Array; Low-Frequency Aperture Array). In fact, the receiving chain is based on an antenna element with large field-of-view, Radio-over-Fiber technology for data transportation and digital back-end based on FPGA.

Additionally, one of the main goal of all MAD campaigns was to verify the use of an Unmanned Aerial Vehicle (UAV) as source in far-field for characterization and calibration of small low-frequency aperture arrays in their operative conditions (e.g. on the ground, with mutual coupling effects, etc.).

MAD is part of a technological research project funded by INAF and mainly conducted by INAF-IRA aimed to increase expertize in the framework of the SKA project and in particular of the LFAA where INAF plays a key-role in several components of the system. The core design documents issued by the SKA Organization office (Baseline Design document, SKA1 Level 0 Requirements, Level 1 Requirements and Concept of Operations) can be found in [1].

The technical and research staff involved in the project include the following research institutes and Universities: Polytechnic of Turin, CNR-IEIIT and INAF-OAA.

During this session, we were pleased to have Stefan Wijnholds from ASTRON attending the measurements who significantly contributed to the discussions and the results analysis.

MAD-3 represents the chronological third measurement session and it was performed in the week May, 19-23, 2014. The previous sessions, MAD-1 and MAD-2 took place on July 2013 and October 2013 respectively. MAD-2 is fully described in [2] as technical internal report, whereas a selection of the main results have been presented at an international conference [3]. The MAD-1 campaign was preceded by the test session mini-MAD, carried out on June 2013 and aimed to check the functionality of the whole system for a single baseline.

We underline that the UAV system for antenna pattern measurement was initially studied to reach the goal of AAVS0 (embedded element pattern measurement) during the summer 2012 considering Vivaldi 2.0 elements.

This document is aimed to provide a general overview of all the technical aspects connected to MAD-3, without exceeding too much in the details. References have been indicated in case more information are needed. This report has been written with also the objective to be useful for the preparation of the SKALA-AAVS0 measurement to be held in Cambridge in September 2014.

The report is organized as follows: Section 2 highlights the MAD-2 experience and identifies the goals of MAD-3. Section 3 gives a description of the hardware and software implemented in MAD-3. Section 4 and 5 describe the hexacopter system and the flight strategies, respectively. Section 6 is addressed to the simulation results, whereas section 7 to the experimental results. The last section of the report deals with conclusions and future developments.

2. Open points from MAD-2 and objectives for MAD-3

The MAD system combined to the novel application of a hexacopter for measuring its performance includes several different electronic equipment. Of course, each electronic part/instrument can present some problems during the overall measurement campaign causing major or minor failures to the whole campaign. Therefore, specific attention has been addressed to have a reliable system in each sub-component.

A list of the main problems and lessons learned raise during MAD-2 follows:

- The total station requires time for configuration and calibration (definition of the reference system). Moreover, it can have a significant drift in its time reference, therefore it should be synchronized at the beginning of each flight. These problems have been overcame using a differential GPS/GNSS measurement scheme: with one GNSS receiver on the hexacopter and one GNSS receiver on the ground.
- The flight strategy should be carefully defined at least one-week before the measurement campaign in order to allow the preparation of the files containing the UAV flying paths.
- The RF signal generator on the UAV should be turned off after landing in order to save batteries. However, it is helpful to check the presence of the RF signal after turning on, using either a spectrum analyzer on the field or the back-end itself.
- Analog amplitude calibrations require a lot of “manual work”. Therefore, a new automatic procedure should be implemented for MAD-3.
- All the electronic components from the antenna port to the back-end should be debugged and tested before the measurement campaign with signal generators and splitters.
- Effect of cables from the receiver outputs to the input of the A/D converters has been tested [2].
- A better organization of the team involved would be beneficial.
- The usage of ASCII files for data transfer slows down the procedure.
- The elaboration software should present the data in a very complete and effective way, in order to simplify both the system testing and the measurement interpretation.
- The post-processing of the data revealed some asymmetries of the E-plane patterns. It was assumed that this fact was due to the presence of the Northern Cross and other obstacles around the array. Later on, the symmetry of the radiated pattern of the UAV source has been investigated, finding some related issues.
- The z-coordinate measurement from the aerial photogrammetry was not enough accurate.
- The quantization noise in the correlator and beam-former outputs needs to be investigated by numerical simulations and comparison between old and new back-ends data.

Concerning the main objective of the MAD-3 campaign, these are listed hereafter:

- Verify the upgrade in the measurements system with the differential GNSS/GPS tracking system instead of the total station.
- Increase the accuracy of array photogrammetry especially in the z-coordinate.
- Test the automatic calibration of the analog chain.
- Test the new back-end system.

- Test a calibration method based on a stationary flight (called “phase snapshot”), instead of using “fringe fitting”.
- Measure embedded element patterns and beams also in the H-plane.
- Test a new balun for the transmitting antenna to improve the symmetry of the radiated pattern in the E-plane.
- Verify the array simulations with new more accurate measurements.
- Test the efficiency of the people arrangement and organization scheme.
- Acquire the full correlation matrix and raw data from each antenna (before correlation) for the imaging and off-line beam-forming test.

3. MAD-3 hardware and software configuration

3.1 Array geometry

The Medicina Array Demonstrator is a 3x3 regularly spaced array composed by Vivaldi v2.0 antennas, operating in dual polarization. The array is arranged in a rhomboidal configuration, as illustrated in Fig. 1, equal to the distribution adopted in MAD-2.

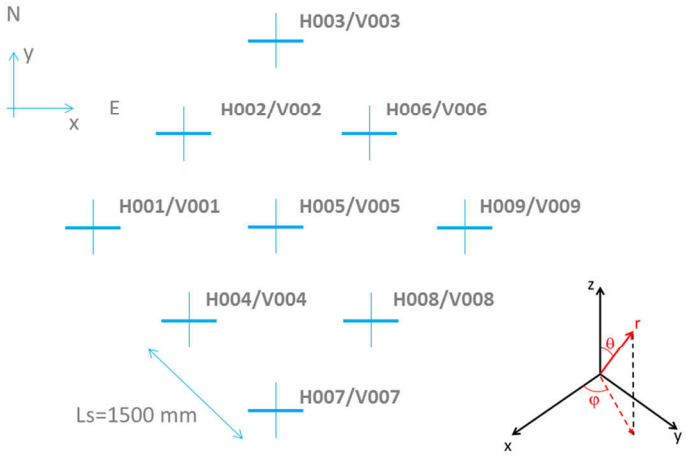

Fig. 1 – Array geometry. Bold and thin lines represent the horizontal and vertical polarization, respectively.

The theoretical antenna positions, expressed in the ENU local reference frame (x, y, z-axes toward East, North and Zenith, respectively), are shown in Table 1 together with the real positions measured with the photogrammetry technique and the reciprocal differences. The origin of this frame is set in the central element of the array (antenna V005/H005) at the top of the optical marker.

The antenna deployment procedure, described in [2], gives a relative position accuracy better than half a centimeter along each axis.

Antenna ID	X_ideal (m)	Y_ideal (m)	Z_ideal (m)	X_real (m)	Y_real (m)	Z_real (m)	ΔX (m)	ΔY (m)	ΔZ (m)
V001/H001	-2.121	0.000	0.000	-2.122	-0.002	0.005	-0.001	-0.002	0.005
V002/H002	-1.061	1.061	0.000	-1.059	1.057	0.004	0.002	-0.004	0.004
V003/H003	0.000	2.121	0.000	-0.002	2.128	0.004	-0.002	0.007	0.004
V004/H004	-1.061	-1.061	0.000	-1.054	-1.055	0.002	0.007	0.007	0.002
V005/H005	0.000	0.000	0.000	0.000	0.000	0.000	0.000	0.000	0.000
V006/H006	1.061	1.061	0.000	1.057	1.070	0.004	-0.004	0.009	0.004
V007/H007	0.000	-2.121	0.000	-0.001	-2.127	-0.002	-0.001	-0.006	-0.002
V008/H008	1.061	-1.061	0.000	1.059	-1.066	0.001	-0.002	-0.005	0.001
V009/H009	2.121	0.000	0.000	2.117	0.000	0.004	-0.004	0.000	0.004

Table 1 - Coordinates of the antenna centers. From left side: ideal positions (columns 2, 3 and 4), coordinates given by photogrammetry in local reference system (columns 5, 6 and 7) and errors in three different directions (columns 8, 9 and 10).

MAD has been installed inside the Medicina radioastronomical station area, near to the NS arm of the Northern Cross antenna (Fig. 2). This location has several major benefits: it allows the utilization of both the station infrastructures and the already installed BEST-2 receiving chains. Additionally, the antenna distribution on the array benefit of the flatness of the terrain. Although the Vivaldi v2.0 antenna covers a frequency range from 70 to 450 MHz, in order to exploit the existing facilities the operative frequency of MAD-3 campaign was chosen to be near 408 MHz. During MAD-2 we experienced that the big metallic structure of the Northern Cross antenna, which is quite close to the array, affects the element beam pattern giving a fast ripple in the curves. Anyway, this contribution can be neglected at this stage.

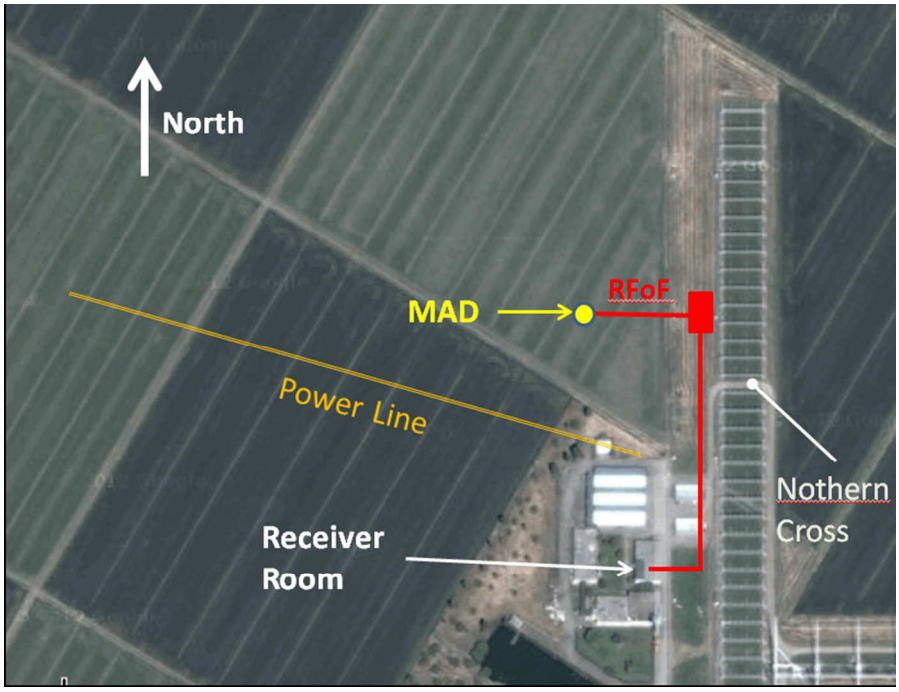

Fig. 2 - Aerial view of the MAD location area inside the Medicina radioastronomical station.

The photogrammetry measurement was performed during the first day with two flights at different heights above ground using a marker placed on top of each antenna. This measurement was done to accurately

know the coordinates of the centers of each antenna with a mm-accuracy. More details on this measurement are in [4]. It is worthwhile mentioning that the photogrammetry values in table 10 of [4] are slightly different to those reported in Table 1, due to a further elaboration performed by the staff of the Polytechnic of Turin. Anyway, all the results shown in this report have been evaluated by using the position data of Table 1.

3.2 Antenna and receiver

The antenna of MAD-3 is a dual-polarized Vivaldi v2.0 developed by CNR-IEIIT. It basically provides a suitable matching level from 70 to 450 MHz (and more) and an isolation between the two orthogonally polarized channels (equal to the cross-polarization at zenith) more than 45 dB owing to the symmetry of the antenna. Other features of the antenna are: it does not require a ground plane; the sky coverage is consistent with the ±45° from the zenith requirement imposed by the SKA-AAVP program.

The opposite arms of each antenna are connected to a robust, 50Ω single ended LNA (Low Noise Amplifier) which has been manufactured by INAF-IRA [5]. The LNA, which is one of the most important component of the front-end circuitry, was designed to assure large flexibility in the choice of the antenna and of the cabling options. Some more technical details on the LNA are: DC voltage = 3 V, current = 60 mA, good noise performance (Tn < 30 K from 100 to 350 MHz) and dynamic range (OIP3 > +30 dBm; OIP2 > +48 dBm).

After the LNA, an analog RF-to-Optical converter transmits the signal through a single-mode optical fiber [6], which is a technology candidate for potential use in SKA-LFAA. The electronics of the front-end, i.e. LNA and optical transmitter together with the batteries for the power supply, have been packaged inside the antenna thickness thus obtaining a low-cost easy-deployable structure with an optical output. The effective battery duration is about 17 hours and 19 hours for the LNA and TX-O, respectively.

On the other side of the optical link, a second part of the RF circuitry called receiver is located inside a shielded and protected environment close to the digital back-end.

More technical details on the analog circuitry can be found in [7], [8] and [9].

3.3 Digital back-end

3.3.1 Firmware Architecture Description

The digital back-end for the MAD experiment has been developed using the ROACH-1[1] CASPER[2] board which is a XILINX VIRTEX-5 FPGA integrated on a mainboard populated of many peripherals such as 4x CX4 10Gbps high-speed serial connectors, 10/100/1000Mbit RJ45 Ethernet, DDR2 DRAM DIMM, 2x 2M x 18-bit QDRII+ SRAMs and much more (Fig. 3).

The aim of the digital back-end is to acquire the analog signals coming from the Vivaldi antenna array and to produce the array beam in both polarizations and to calculate the correlation products. A brief description of the firmware developed and used for MAD-2 measurement campaign in reported in [2].

[1] Reconfigurable Open Architecture Computing Hardware - https://casper.berkeley.edu/wiki/ROACH

[2] https://casper.berkeley.edu/

For MAD-3 experiment, the firmware has been upgraded with a new part (operating in parallel to the existing one) in order to improve mainly two aspects of the previous version: reduce quantization effect especially for low level signal power and provide configurability of the baseline set for correlation:

1. Quantization effect. After phase compensation block, data is no longer quantized but it is processed by correlator and beam-former with its full binary representation; the only quantization is applied before sending data through 10 GbE network interface: in this case data is quantized to 64 bit complex (the older part produces 32 bit complex output data).
2. Baseline set of correlation products. The new part is more flexible than the previous one: in fact, it is possible to select via software the correlations to be calculated. With the old part, only a well-defined subset of 8 baselines is processed by correlator, according to the phase calibration "fringe fitting" procedure.

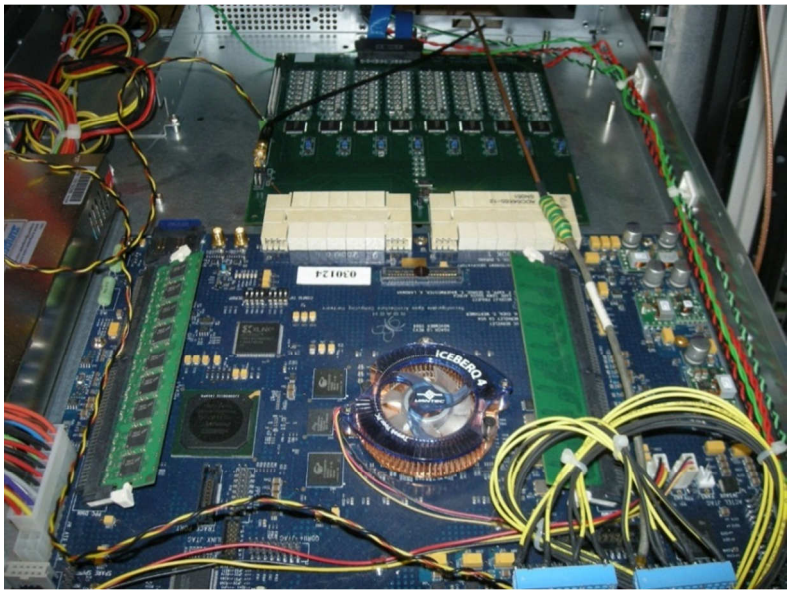

Fig. 3 - ROACH board with the 64 input ADC connected via two Z-DOK connectors.

All hardware devices and their interconnections composing the digital back-end used for MAD-3 measurement campaign are depicted in Fig. 4.

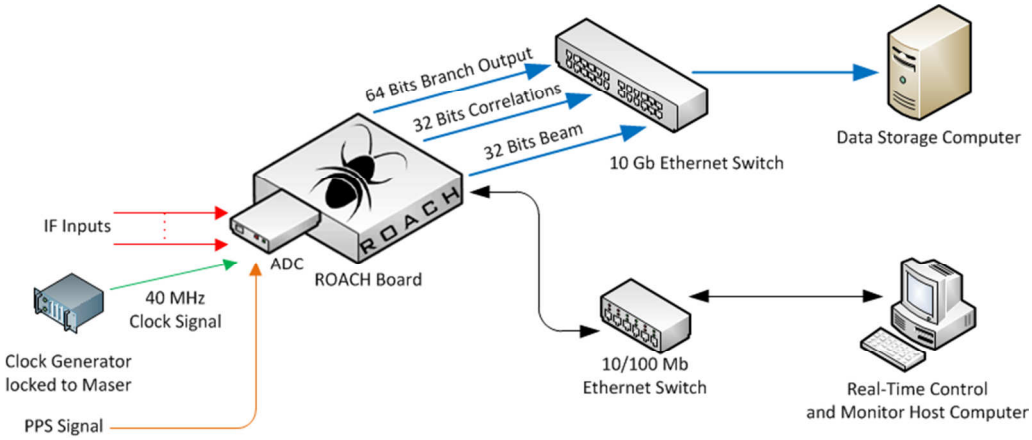

Fig. 4 - Digital back-end scheme

Fig. 5 represents in a very simplified scheme the main processing blocks implemented in the firmware: the new added part is marked with color. In the first raw there are the same blocks of the previous version and no changes have been introduced: A/D conversion, frequency channelization, amplitude and phase equalization. Then the frequency channel bin of the CW signal (408 MHz) transmitted by the drone, relative to all antennas and polarizations (9 ant. Pol V + 9 ant. Pol H), is stored by a buffer formed by FIFOs and a Dual Port RAM pair.

As said before, data buffered into memory after equalization stages is no more rescaled and quantized but it is taken as is with its full binary representation, i.e. 70-bit complex instead of 16-bit complex. Specific control logic drives the reading of the Dual-Port RAM with the opportunity to choose, by software user commands, which couple of antennas will be cross-correlated. Output data from buffer is processed by three main blocks: *(i)* an accumulator calculates separately the sum of the signals of the same polarization providing the beam for pol. V and the beam for pol. H (BEAM block), *(ii)* a multiplicator calculates all auto-correlations for both pol. V and pol. H (AUTO block) and *(iii)* finally another multiplicator is used to compute the selected correlation products. Another buffer is necessary to collect and arrange data in packets before sending it to data storage computer through 10 GbE network. Output data from both correlation and beam-forming blocks are quantized to 64-bit complex: this allows to compare the quantization effect over the digital chain with the results obtained with the older part of firmware (32-bit complex). Note also that output data stream of this new branch is sent through only one network interface (for the old branch there were two).The principal features of the two parts of firmware are summarized in Table 2 (the main differences are underlined).

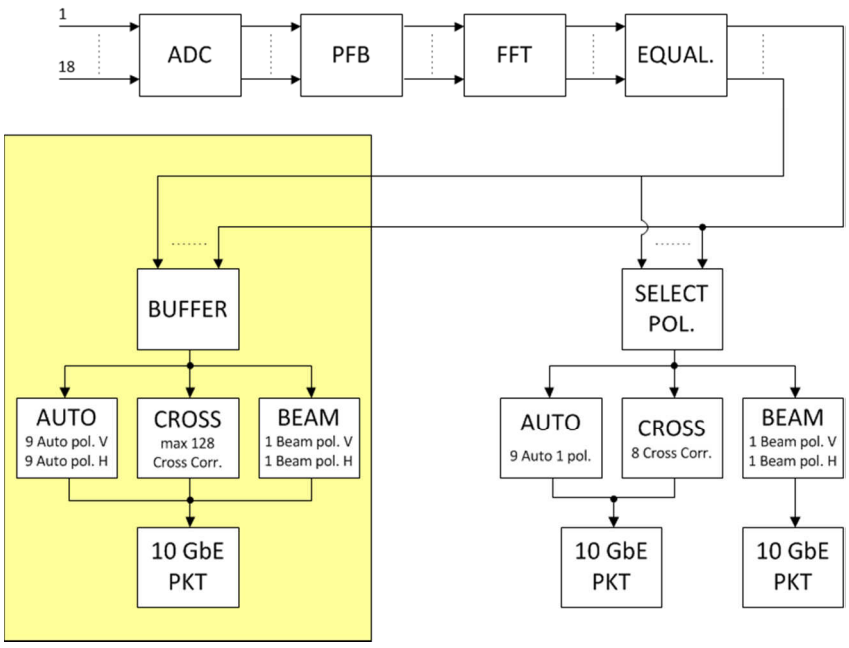

Fig. 5 - Block diagram representing the main processing blocks implemented in the upgraded version of firmware.

An issue of this high performance digital back-end is represented by the data transfer to the data storage computer. The 10 GbE link is the limit for the bandwidth of the physical layer together with the PCI-Express network card and the disk speed. A typical computer with a SATA-2 disk can achieve a read/write speed of 100-150 MB/s. These numbers are affected by the running processes of the operating system and they are not constant. By the way for the 32-bit system a rate of about 1.5 MB/s would be enough.

However, there are latencies caused by the (software) save script routine which should be considered with great attention because they affect very much the effective rate. This becomes a big issue when doubling the rate and the data volume in the 64-bit system: for this reason we decided to use a workstation as data storage computer having a set of disk in a RAID configuration able to achieve read/write capabilities of 350 MB/s. Unfortunately we got missing packets again and further studies on the software point of view must be made. This workstation has been very important during the flight when the full correlation matrix was calculated and 56 parallel data streams were collected (9 Auto H + 9 Auto V + 36 Correlation + 2 Beam): in that case such a high performance storage system was necessary.

Firmware Specifications			
	32 bits branch	**64 bits branch**	
ADC Sampling Rate	40	40	Msps
ADC Sampling Precision	12	12	bit
Antenna #	9	9	Dual Pol.
Polarization #	2	2	
PFB	4 tap FIR + 2048 point FFT	4 tap FIR + 2048 point FFT	Radix-2 Biplex Real FFT
Frequency resolution	19.5	19.5	kHz
Time resolution	51.2	51.2	µs
Quantization after FFT	36	36	bit
Quantization after Amplitude Eq.	36	36	bit
Quantization after Phase Eq.	16	70	bit
Effective Output Data Rate[3]	-	45[4] - 70[5]	Mb/s
Correlator			
Auto Correlations	9	18	
Cross Correlations	8	16[4] - 36[5]	
Quantization	32	64	bit
Effective Output Data Rate[3]	11.25	-	Mb/s
Beamformer			
Beams	2	2	1 H Pol., 1 V Pol.
Quantization	32	64	bit
Effective Output Data Rate[3]	1.25	-	Mb/s

Table 2 – 32 and 64 bits firmware branch specifications.

[3] The effective output data rate is calculated without taking into account of the 8 bytes packet header which depends on the packet size set (~0.02% in the case of MAD-2 set up with 648 as packet length).
[4] This is the case when the number of computed cross-correlations is restricted to a well-defined baseline subset according to the phase calibration "fringe fitting" procedure (see [2]).
[5] This is the case when the Full Correlation Matrix is calculated.

3.3.2 Back-end Data Synchronization

The ADC receives the clock signal from a signal generator that is locked to the ultra-stable 10 MHz sine wave provided by the Hydrogen Maser. This precision frequency reference is used to generate the PPS signal that is distributed also to the ADC board. The host computer is synchronized via a local NTP server with the station time (UTC), which is in turn synchronized with a GPS receiver and locked, for its stability, to the Hydrogen Maser. Note that the station time is aligned to PPS signal with very good precision.

During the initialization phase, after an ADC alignment test, the acquisition start time is set by the user in the host computer. As soon as the station time has an (integer) increment of the seconds, that means a PPS signal has been just received into the firmware, the host computer sends a "sync arm" signal to the firmware. This signal arrives certainly before next PPS signal. When this PPS signal goes high, a “master reset” signal is triggered into the firmware and it causes the reset of all synchronous components (counters, registers, …). Moreover the same PPS is taken as the initial reference T_0 time, which is stored to local registers and attached to the observation file header. Every data packet has a 8-byte counter header which allows to compute in post-processing the acquisition time of each sample. This procedure is robust enough to guarantee very high time accuracy for each stored data even in case of packet loss.

In Fig. 6 it is reported a very simple scheme representing the steps for the synchronization of ROACH board, host computer and data storage computer.

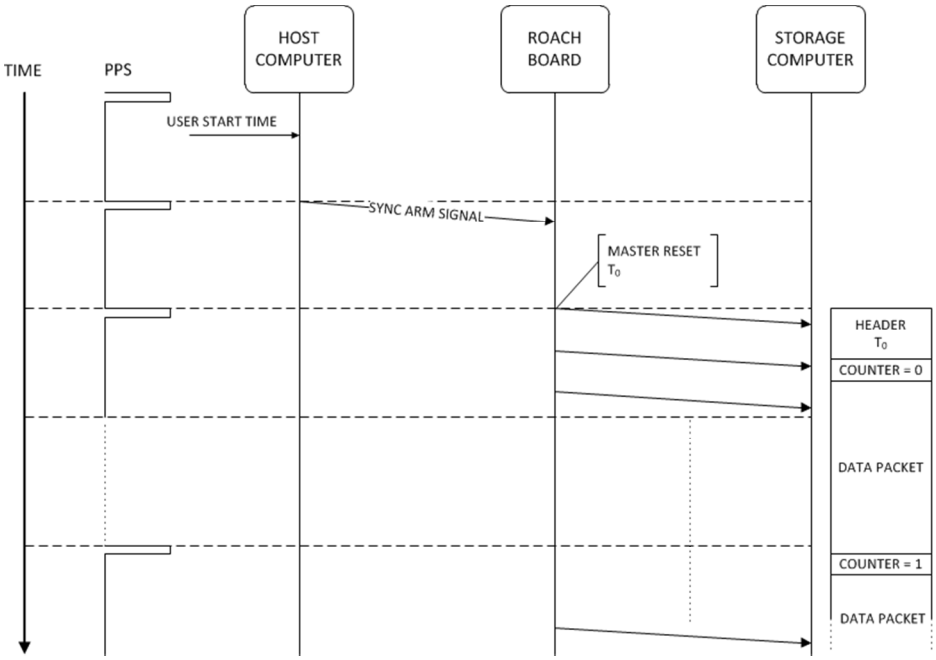

Fig. 6 – Back-end data synchronization scheme.

3.3.3 Comparison between 32-bit and 64-bit firmware outputs: preliminary results

The performance of the new back-end firmware were tested on the field. The 408 MHz CW signal from the transmitter on board of the hexacopter was disconnected from the antenna and connected to a variable attenuator, a splitter and then injected in the LNAs of two receiving chain (H005 and H009 antennas) (Fig. 7).

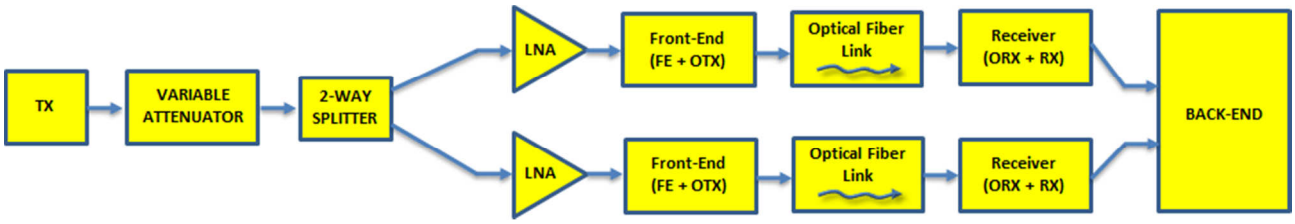

Fig. 7 – Scheme of the test system

The correlations, performed in parallel by the two branches of the same firmware, were compared in terms of amplitude (Fig. 8a) and phase (Fig. 8b) for different signal powers ranging from 0 to -10 dBm (measured at ADC input) with 1 dB steps. The spikes visible in the plots are due to the commutation of the power level in the variable attenuator.

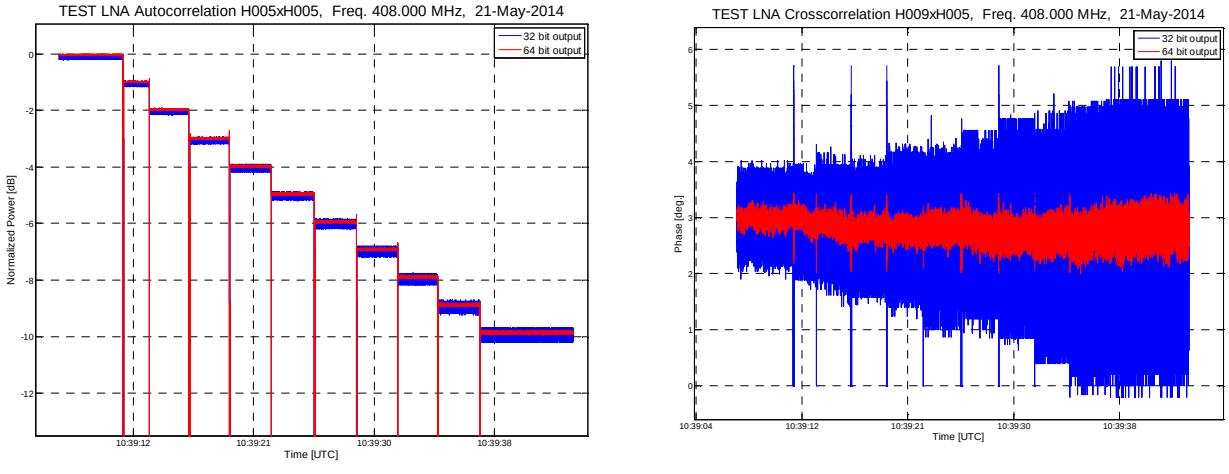

(a) (b)

Fig. 8 – (a) Normalized received power of the H005 element calculated with 32-bit (blue) and 64-bit (red) firmware outputs; (b) Relative phase between H009 and H005 elements calculated with 32-bit (blue) and 64-bit (red) firmware outputs

The 64-bit firmware output has a better behavior than the 32-bit one in terms of standard deviation of phase and amplitude, especially at lower power levels, where the quantization errors become more relevant.

However the 32-bit output firmware has been preferred for the MAD-3 data analysis because the 64-bit output firmware was not yet completely debugged, taking into account that errors for not integrated values are greater as mentioned before. From the data plotted in Fig. 8 it is possible to demonstrate that the average values of amplitude and phase are almost the same in both firmware firmware (in the worst case the mean values of phase and amplitude differ of only 1.3% and 0.07 dB, respectively).

3.4 Software

In order to optimize the data rate and to reduce the packet loss risk, the software (developed by INAF-IRA) installed on the data storage computer acquires and saves the data incoming from the digital back-end in a binary format containing all the correlation products and the time information. A similar format is also adopted for the beam-former output.

The data post-processing of the back-end data is performed by a dedicated number of procedures developed by the INAF-IRA team in IDL (Interactive Data Language) environment. The main tasks of these tools are the following:

- Decoding and conversion of the raw binary data produced by the correlator and beam-former.
- Calculation of the time vector associated to data.
- Data integration.
- Calculation of the amplitude corrections by means of the "equalization" or the "power pattern simulation fitting" techniques.
- Calculation of the phase corrections using the "fringe fitting" or the "phase snapshot" methods.
- Preliminary array beam de-embedding.
- Generation of the output file containing the complex gain vector.

The same tool pack is able to perform other secondary tasks as data filtering and extraction/conversion, preview of the post-processing results, interpolation of the hexacopter positions, etc.

Some algorithms were derived from those used in the MAD-2 campaign, however many optimizations were implemented for MAD-3 in order to both automate the whole process and increase the performances by mean of multi-threaded algorithms on multi-processor systems.

Finally, other post-processing codes were developed by the CNR-IEIIT for the embedded pattern and the array beam analysis and for the comparison with the electromagnetic simulations.

4. Hexacopter System

4.1 General description of the drone

The hexacopter, which is shown in Fig. 9, is based in the control board Mikrokopter KGPS ver. 1.0 equipped with the u-blox 6S sensor [4]. It allows for an arbitrary GNSS-controlled autonomous flight with a maximum duration of 15 min. A remote pilot is needed for the takeoff and landing operations.

The UAV control board also provides a stable orientation of the hexacopter during the overall flight. The three orientation angles (bearing, pitch, and roll) that are measured with its internal Inertial Measurement Unit (IMU) are available for post-processing with an accuracy of about 2 deg.

The hexacopter has been equipped with a continuous-wave RF signal generator based on a PLL synthesizer that can operate from 160 MHz to 4.4 GHz, with a maximum power level of 8 dBm. A selectable frequency divider (up to ÷32) allows to reach 5 MHz as minimum frequency. In our experiment, the frequency divider was set to ÷4 and consequently the maximum power level is reduced to 5 dBm.

Two telescopic monopoles are connected to the generator with an integrated broadband balun. The total dipole length is adjusted for each operative frequency to obtain a good impedance matching at the unbalanced port of the balun. The six arms of the hexacopter are made of aluminum. Therefore, they have been considered as a part of the test source. The generator metal package is completely symmetrical in order to avoid spurious cross-polarized contributions. The generator can be programmed from an external PC connected to USB port and it can be used with or without a frequency divider.

The two skids are instead made of wood and plastic to reduce the interaction with the dipole.

The relative orientation of the source dipole with respect to the AUT on the ground corresponds to the bearing angle of the UAV, which can be set as a variable of the flying path.

An optical retro-reflector is mounted under the hexacopter for an accurate optical tracking of the UAV during the overall flight by means of a motorized total station; however, in this campaign it was not used anymore being replaced by the differential GNSS.

Fig. 9 - Hexacopter equipped with RF transmitter and telescopic dipole.

4.2 GNSS system for positioning tracking

One of the main difference in MAD-3 with respect to MAD-2 is that the total station was not used anymore. The flights were tracked (position versus time) by mounting a double-frequency GNSS receiver on the hexacopter and using a differential cinematic technique called PPK (Post-Processing Kinematic). The GNSS card is connected to an active GNSS antenna double-frequency able to receive signals coming from GPS, GLONASS and Galileo. The raw data are stored in a SD card connected to the OEM board. A ground station is provided by a Smart Antenna which has been located in two well-known positions.

The GNSS sampling is set to 1 Hz. As a next step, a higher sampling rate (5 Hz) will be implemented.

During the measurement, the original GNSS receiver on board of the drone was changed with a back-up one due to some electrical failures.

The new technique based on the GNSS receiver requires to acquire GNSS data by: *(i)* hold on the hexacopter at the starting point for 2-3 minutes before starting the flights, *(ii)* hold on the hexacopter some more seconds on the waypoints during the flight and *(iii)* hold on the hexacopter 2-3 minutes after the flight.

The positions of the hexacopter are synchronized to the local time as given by the GNSS system.

The GNSS measurements are originally generated in a no standard format and are expressed in an absolute geocentric reference frame. Therefore, the group of the DIATI-Polytechnic of Torino developed a post-processing software able to:

- Convert the hexacopter coordinates in the local ENU reference system used for the array.
- Convert the GPS time in UTC (the same of the back-end data).
- Produce the output data file in the standard format suitable for the post-processing tools.

5. Flight Strategies

Different flight strategies were implemented for optimizing each type of measurement/operation:

1) **Analogue equalization**: stationary flight at zenith divided in two parts: with Tx compass 0 deg for the V-pol and Tx compass 90 deg for the H-pol. The attenuators were automatically adjusted to have ~0dBm signal at ADC input with hexacopter at zenith. This value was a trade-off between the receivers linearity and the ADCs sensitivity.
2) **Check of the analog levels**: "L-shape" trajectory (passing at zenith) with Tx compass 0 deg along the NS branch and Tx compass 90 deg along the EW branch. At the path's extremities, the hexacopter reaches the maximum distance that is expected in the campaign flight plan in order to check di minimum signal level input received by the antenna co-polar pattern.
3) **Amplitude and phase calibration with "snapshot" method**: stationary flight at zenith divided in two parts: with Tx compass 0 deg for the V-pol and Tx compass 90 deg for the H-pol.
4) **Embedded element pattern measurement**: "X-shape" trajectory, passing at zenith, along the antenna principal planes with either Tx compass 0 deg for the V-pol or Tx compass 90 deg for H-pol.
5) **Array beam pattern measurement**: same strategy used for the embedded element pattern.
6) **Off-line beam-forming and imaging:** stationary positions at different ϑ angles followed by a NS direction scan.

All the trajectories have a constant height from the ground large enough to fulfill the far-field condition for the array. Initially the hexacopter height was 70 m, then it was raised at 100 m in order to reduce the angular errors due to the inaccuracy of the hexacopter position measurements.

In order to reach a maximum theta-angle of 45 degree, the maximum distance from the zenith position during the rectilinear trajectories was equivalent to the hexacopter height above ground. In particular, the details of the flights cited in this report are shown in Table 3.

ID code	Starting date/time [UTC]	Trajectory (ENU) [m]	Tx Comp. [deg]	Speed [m/s]	Purpose	Note
134_1	22/05/2014 10:30:14	Stationary at zenith: (0,0,100)	0	0	Automatic analogue equalization in V-pol	
134_3	22/05/2014 10:34:02	Stationary at zenith: (0,0,100)	0	0	Calculation of amplitude and phase coefficients in V-pol	
134_4	22/05/2014 10:34:57	Stationary at zenith: (0,0,100)	90	0	Calculation of amplitude and phase coefficients in H-pol	
331_1	22/05/2014 16:05:04	Rectilinear from S to N (0,-100,100) → (0,100,100)	0	1.5	- Verification of the array calibration in V-pol by fringe patterns - Embedded element patterns (E-plane in V-pol)	Array calibrated with coefficients calculated from 134_3 and 134_4
631_1	22/05/2014 16:24:07	Rectilinear from E to W (100,0,100) → (-100,0,100)	90	1.5	- Verification of the array calibration in H-pol by fringe patterns - Embedded element patterns (E-plane in H-pol)	Array calibrated with coefficients calculated from 134_3 and 134_4
142_1	23/05/2014 07:25:01	Stationary at zenith: (0,0,100)	0	0	Calculation of amplitude and phase coefficients in V-pol	
142_5	23/05/2014 07:33:34	Rectilinear from N to S (0,100,100) → (0,-100,100)	0	1.5	Fringe patterns measurement before calibration	Not calibrated array
441_1	23/05/2014 08:13:36	Rectilinear from N to S (0,100,100) → (0,-100,100)	0	1.5	Array and embedded element patterns (E-plane in V-pol)	Array calibrated with coefficients calculated from 142_1
441_2	23/05/2014 08:15:38	Rectilinear from S to N (0,100,100) → (0,-100,100)	0	1.5	Array and embedded element patterns (E-plane in V-pol)	Array calibrated with coefficients calculated from 142_1
441_3	23/05/2014 08:18:12	Rectilinear from W to E (-100,0,100) → (100,0,100)	0	1.5	Array and embedded element patterns (H-plane in V-pol)	Array calibrated with coefficients calculated from 142_1
541_1	23/05/2014 08:45:46	Stationary at zenith: (0,0,100)	0	0	Amplitude and phase stability in V-pol	Not calibrated array
A41_n	23/05/2014 09:54:18	n = 0,1,2,3,4 stationary flights at: (0,0,100) $\vartheta = 0°$; (0,20,100) $\vartheta \cong 11°$ (0,38,100) $\vartheta \cong 21°$ (0,61,100) $\vartheta \cong 31°$ (0,100,100) $\vartheta = 45°$ n = 5 NS rectilinear scan: (0,100,100) → (0,0,100)	0	0 1.5	Off-line beamforming and imaging in V-pol	- Array calibrated with coefficient calculated from 142_1 - Acquisition of the Full Correlation Matrix and raw data at 64-bit

Table 3 – Details of the hexacopter flights mentioned in the report.

Moreover, since we preferred to maintain the compatibility with the configuration adopted for MAD-2, a subset of 8 baselines (Table 4 and Fig. 10) for each polarization was selected. The selection criteria were to

have the minimum set of baselines necessary to calculate all the phase corrections and, at the same time, to have the maximum fringe frequency pattern along the UAV trajectory. The phase reference antennas were V007 and H009 for the vertical and horizontal polarization, respectively. For both polarizations, the baselines are optimized for the E-plane (rather than for the H-plane).

Vertical polarization (E-plane in NS direction)	Horizontal polarization (E-plane in EW direction)
V007 – V001	**H009 – H002**
V007 – V002	**H009 – H003**
V007 – V005	**H009 – H004**
V007 – V006	**H009 – H005**
V007 – V009	**H009 – H007**
V003 – V004	**H001 – H006**
V003 – V008	**H001 – H008**
V003 – V007	**H001 – H009**

Table 4 - Baselines selected for the MAD-3 phase calibration.

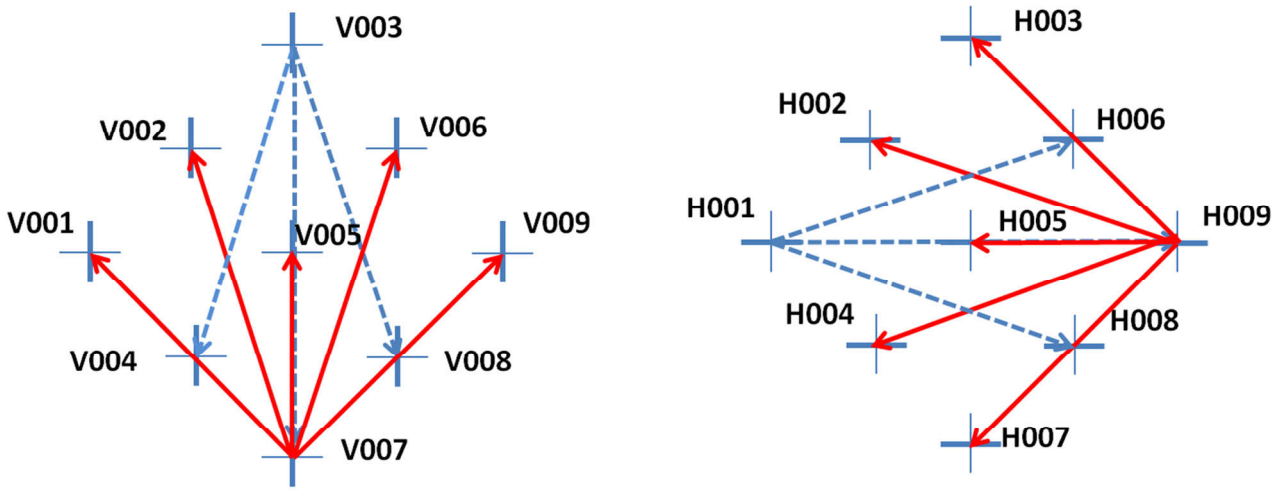

Fig. 10 - Baselines used for the array phase calibration in vertical *(left)* and horizontal *(right)* polarization.

In general, during the pattern measurements, it is important to perform the same quasi-rectilinear path in two passes with opposite direction i.e. both South/North and North/South in order to have some redundancy of the data. This option allows a better understanding of the measurement error produced by the wind.

Finally, the flight A41_n was implemented in order to make an off-line beamforming through the raw data received from each array element and to synthetize the image by means the full correlation matrix. The raw data and the Full Correlation Matrix were simultaneously acquired by the new 64-bit back-end output branch. The A41 trajectory was divided in 6 parts: stationary positions at $\vartheta = 0°, 11°, 21°, 31°, 45°$ followed by a NS scan from $\vartheta = 45°$ to $\vartheta = 0°$. The software able to perform the post-processing of the 64-bit data is under development.

6. Electromagnetic considerations and simulations

In order to extract the required pattern of the antenna under test (AUT) from the received signal at the AUT port (antenna element or array), the Friis equation in [10] is conveniently written as

$$g_{AUT}(\hat{r})M(\hat{r}) = \frac{P_R(\underline{r})}{P_S \cdot g_S(\hat{r},\alpha,\beta,\gamma) \cdot G_R}\left(\frac{4\pi R}{\lambda}\right)^2 \quad (1)$$

where g_{AUT} is the gain of the AUT (unknown of the problem), the unit vector $\hat{r}$ identifies a specific observation direction in the AUT spherical reference system, M is the polarization mismatch, P_R is the measured received power at AUT port, $\underline{r} = R\hat{r}$ is the distance vector from the AUT to the test source measured by the differential GNSS, G_R contains LNA gain, optical link cable losses, receiver gain, etc…. P_S and $g_S(\hat{r},\alpha,\beta,\gamma)$ are the source power and its radiation pattern, respectively. The angles α, β and γ, called bearing, pitch and roll, describe the orientation of the test source measured by the IMU.

The polarization mismatch in Eq. (1) can be written as a function of the polarization vector components of both test source and AUT, relative to the third Ludwig polarization basis [11] in the AUT reference system

$$M = |\hat{p}_S \cdot \hat{p}_{AUT}|^2 = |p_S^{co} p_{AUT}^{co} + p_S^{x} p_{AUT}^{x}|^2 \quad (2)$$

where the superscripts *co* and *x* identify the co-polar and cross-polar components, respectively.

Owing to the two-fold symmetry of the test source, its cross-polar component value approaches zero in its principal planes. Therefore, when $\alpha = 0°$ (co-polar orientation), $p_S^x \simeq 0$ and $p_S^{co} \simeq 1$, hence $M \simeq |p_{AUT}^{co}|^2$. In this case, the first member of Eq. (1) becomes the co-polar pattern g_{AUT}^{co} that can be estimated through the second member of the equation. In other words, the AUT pattern g_{AUT}^{co} is computed by removing the simulated contributions of the source pattern g_S, the path loss and the constants $P_S G_R$ from the measured received power P_R.

An analogous extraction procedure can be adopted for the cross-polar patterns.

The antenna patterns are plotted in a spherical coordinate system as a function of the zenith angle.

The dipole antenna on the UAV has been simulated with CST Microwave Studio to numerically evaluate the antenna pattern g_S.

The measured data of the AUT pattern have been compared to the numerical simulation obtained from CST Microwave Studio. The AUT geometry was introduced in the simulator together with the soil, whose parameters have been taken from (Soil C). At 408 MHz, permittivity and conductivity values are 8 and 0.06 S/m, respectively.

Due to the variations in the hexacopter trajectories with respect to the ideal E- and H-planes, the simulated results have been interpolated along the real path of the hexacopter. Actually, having the MAD-3 antennas a large field-of-view, it would be not strictly necessary to perform this transformation of the source position.

7. Experimental results

7.1 Introduction

In this section, we show the most significant results of the MAD-3 campaign. We shortly list here the main RF settings and targets of the experiment:

- Frequency: 408 MHz.
- Power source level: +5 dBm.
- Only co-polar patterns have been measured (no cross-polar patterns).
- The co-polar patterns have been measured along the E- and H-plane.
- The measurements have been performed for the embedded antenna patterns (section 7.2) and for the array pattern (section 7.4); the array calibration, which is necessary for the array pattern measurements, is described in section 7.3. Finally, further consideration on phase errors are discussed in section 7.5.
- Almost all the measurement have been compared with numerical results.
- In order to prove data repeatability, results obtained in different sessions are plotted together.

7.2 Embedded antenna patterns

Fig. 11 to Fig. 13 show the embedded E-plane and H-plane co-polar patterns of elements V1 to V9. They refer to flight 441_2 and 441_3, respectively, carried out on the 23rd of May 2014.

The measurements show good agreement with the simulations, with some differences between elements, probably due to irregularities of the distance antenna-ground. The ripple is probably produced by scattering sources in the nearby of the array.

Three sub-plots of Fig. 14 show the effect of the UAV orientation correction on the extracted pattern of three different elements. They refer to flight 441_1, which has been affected by high wind. High wind conditions produce a high pitch angle of the UAV (4-8 Deg in this case), which creates a distortion of the measured pattern. This effect is more remarkable in the E-plane, since the gain of the transmitter antenna in the H-plane is more constant. The corrected data are in good agreement with the simulations.

The remaining sub-plots of Fig. 14 show the embedded-element patterns of three elements measured during three different flights. The repeatability of the data is very good.

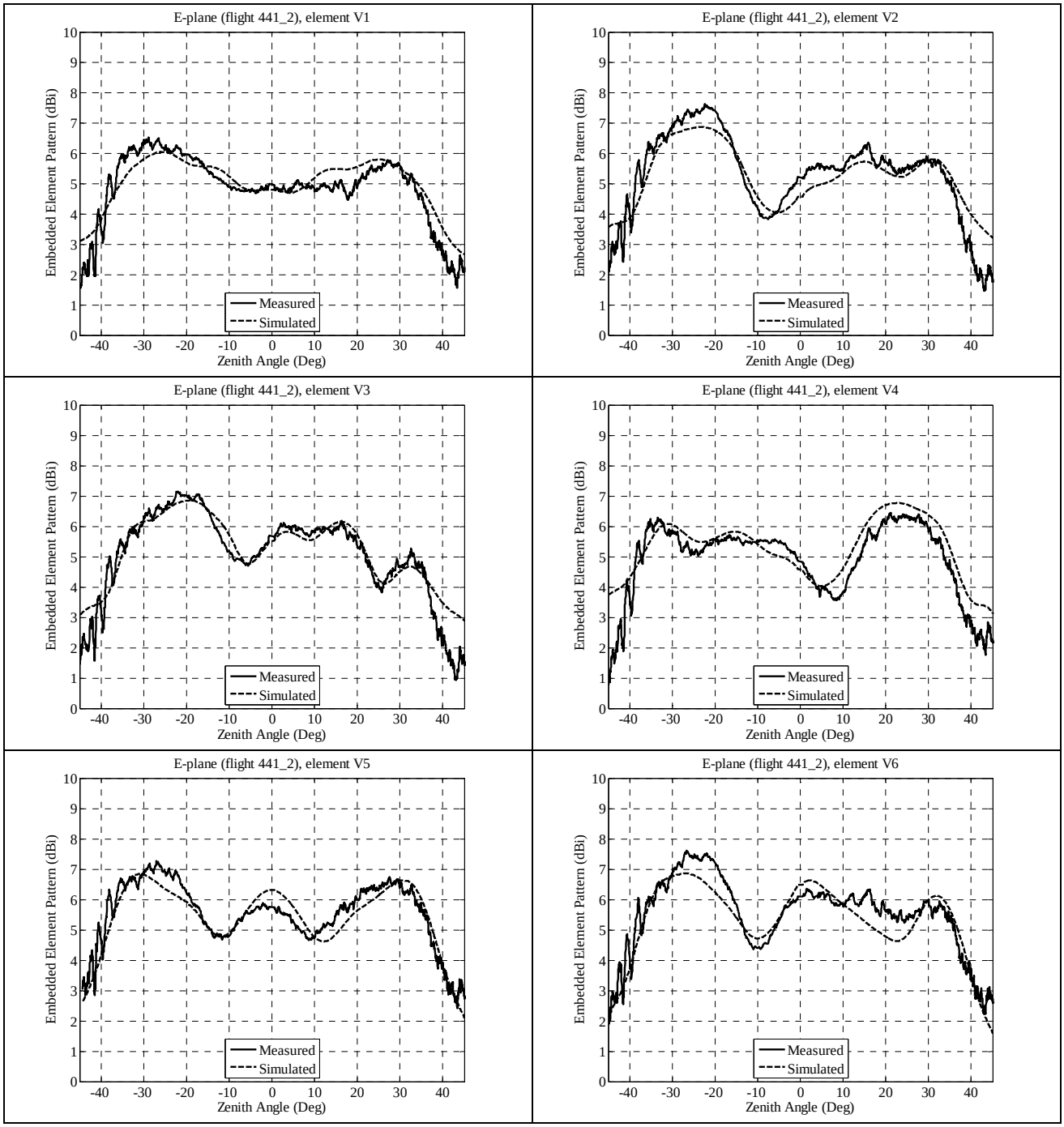

Fig. 11 - E-plane embedded co-polar pattern of elements V1 … V6.

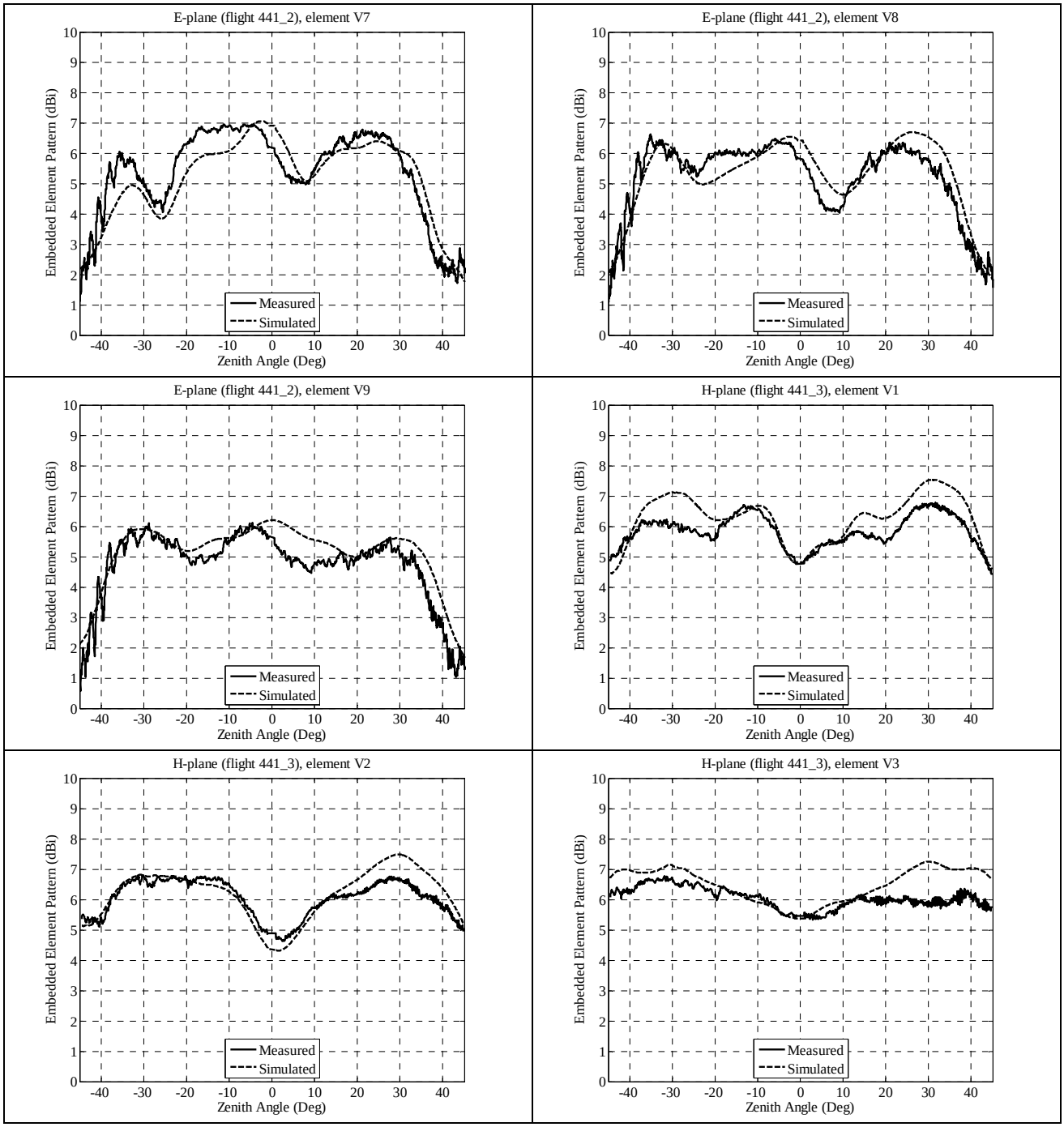

Fig. 12 - E-plane embedded co-polar pattern of elements V7 … V9 and H-plane embedded co-polar pattern of elements V1 … V3.

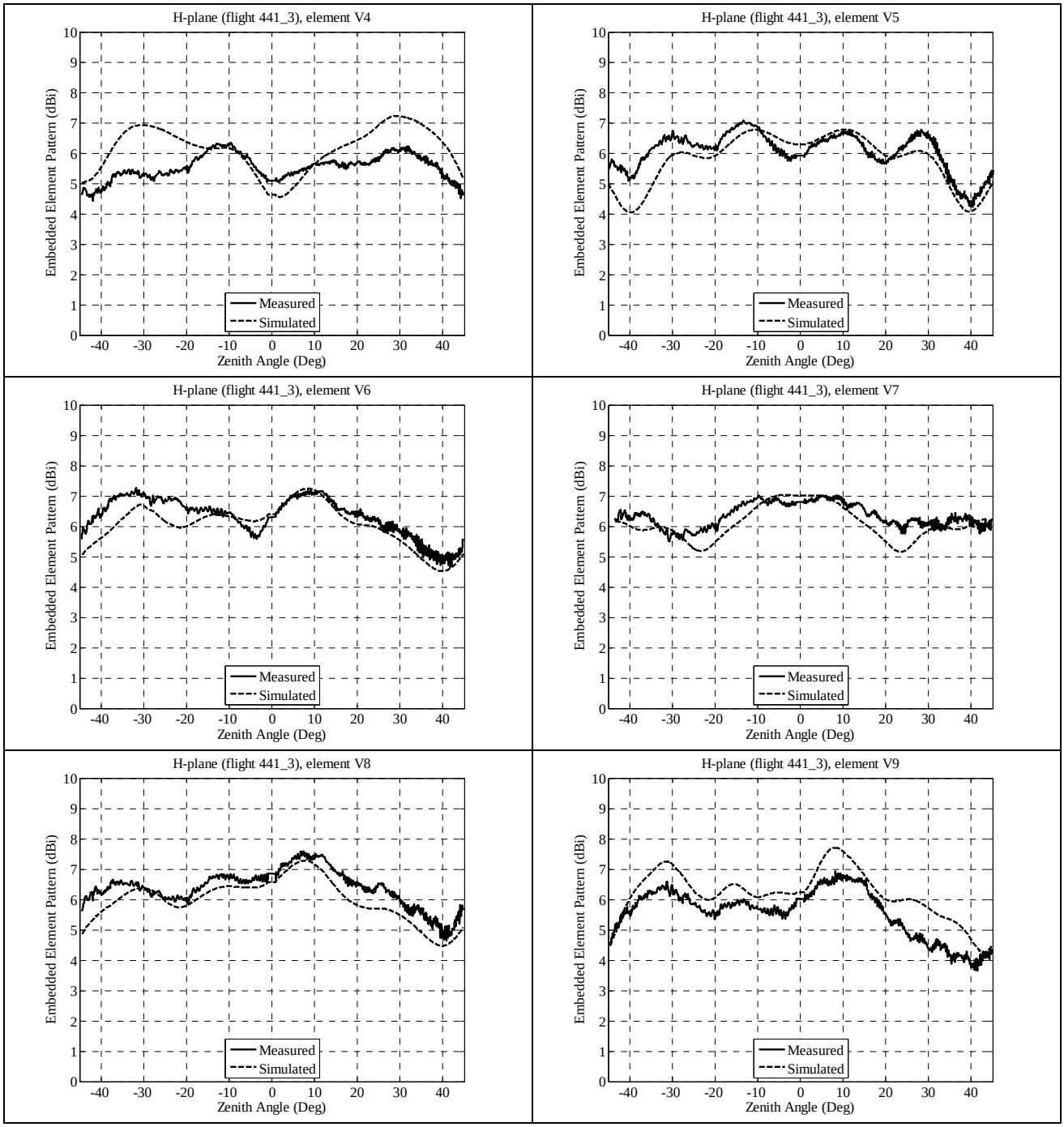

Fig. 13 - H-plane embedded co-polar pattern of element V4 … V9.

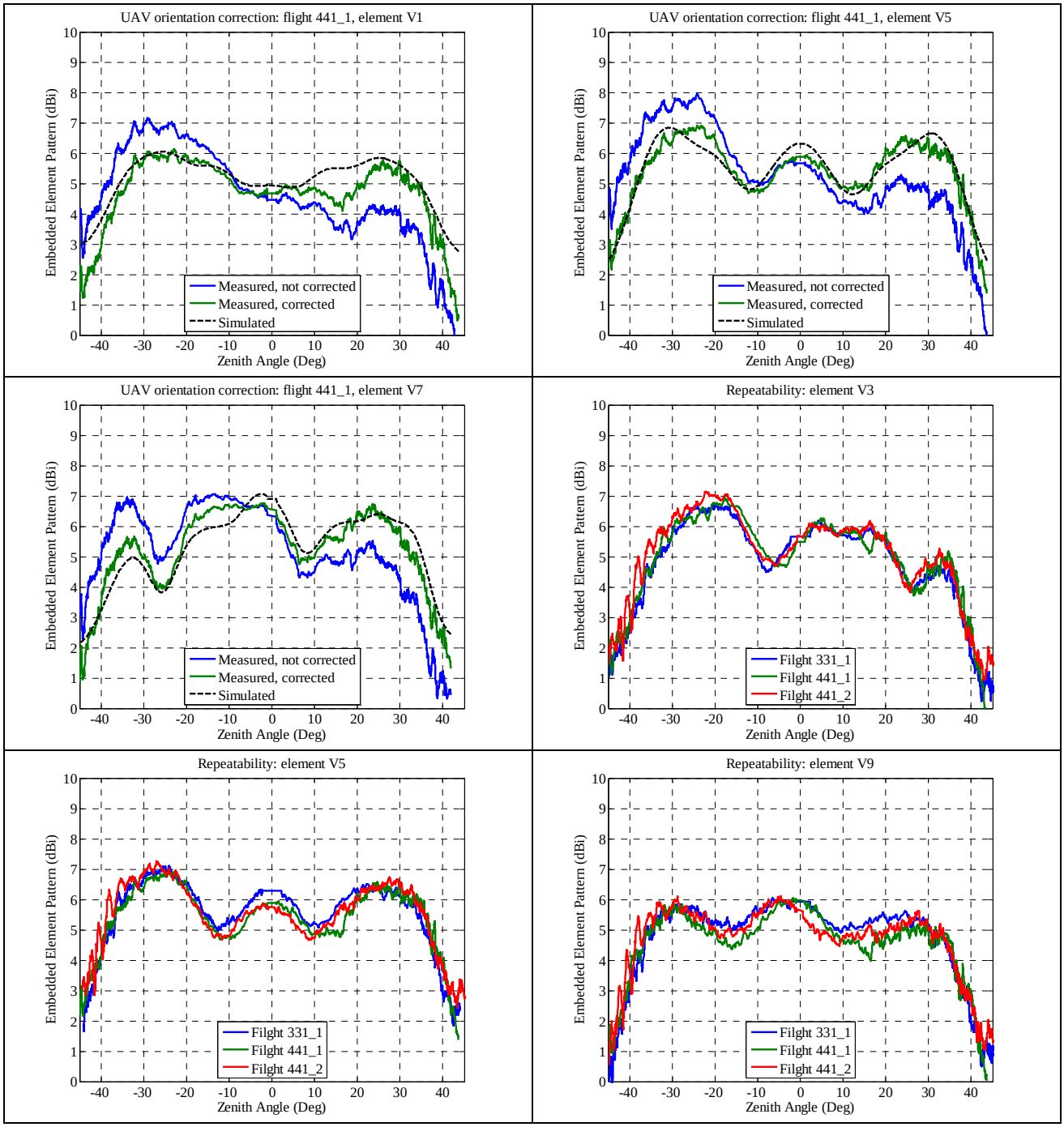

Fig. 14 - Effects of the correction of the UAV orientation angles on the V1, V5 and V7 pattern (first row and left side of second row). Repeatability of the V3, V5, V9 E-plane co-polar pattern (right side of second row and third row).

7.3 Array calibration (amplitude and phase)

Before starting the array operations, a coarse analogue signal power equalization has been performed to check that back-end worked correctly in its linear region (dynamic range from -30 to +10 dBm). A fully automatic equalization system linked to the carrier boards of the BEST-2 receivers was successfully used instead of the semi-automatic system of the previous MAD campaign.

In MAD-3 the amplitude coefficients of each antenna element were calculated in order to have the same received power level with the hexacopter located at zenith. This choice comes from the fact that the array beam produced by the digital beam-former was pointed in that direction. For the array calibration, the hexacopter flew in a nearly zenithal stationary flight at a nominal height of 100 meters. Due to the analogue equalization, the array was almost already calibrated in amplitude and therefore the amplitude corrections were near to unity.

However, the wind and the limited accuracy of the hexacopter navigation system caused the real trajectory, that can be verified only after the flight, to be quite different to that planned (see for example Fig. 15). The real position of the antenna was corrected to remove both the path loss and the transmitting antenna pattern effects (by using differential GNSS/GPS data), but this means that the amplitude and phase calibration is performed not exactly along the zenith direction (as desired) but few degrees off.

As a next step, a more advanced algorithm using the simulated embedded element patterns in combination with a proper flight strategy could be useful in order to improve the amplitude calibration accuracy.

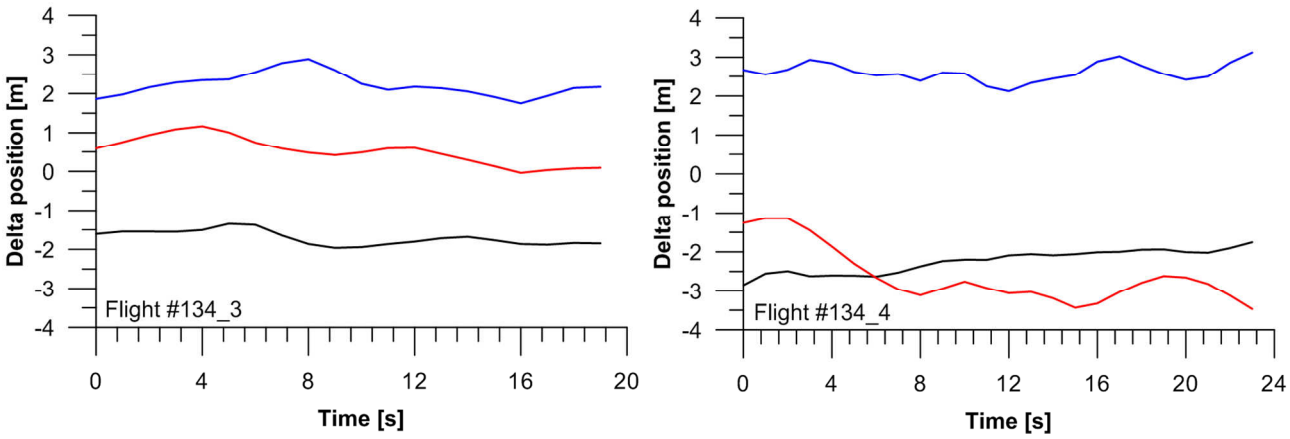

Fig. 15 - Differences between observed and programmed hexacopter coordinates x (black line), y (red line) and z (blue line) for the stationary zenithal flights 134_3 (left) and 134_4 (right).

The same stationary flight allows to calculate the phase corrections for the array calibration. In the phase calibration procedure, one antenna for each polarization is taken as phase reference: $\varphi_{V007} = 0$ and $\varphi_{H009} = 0$.

For each baseline, composed by the elements i, j, the digital back-end produces the complex cross-correlation:

$$R_{ij} = \langle V_i(t) V_j^*(t) \rangle = \frac{A_i A_j}{2} e^{i\phi_{ij}} \qquad (3)$$

So the total relative phase between the elements i, j is given by:

$$\phi_{ij} = atan2\left(\frac{Imag(R_{ij})}{\sqrt{R_{ii}R_{jj}}}, \frac{Real(R_{ij})}{\sqrt{R_{ii}R_{jj}}}\right) \quad (4)$$

Where $R_{ii} = \langle V_i(t)V_i^*(t)\rangle = \frac{A_i^2}{2}$ is the auto-correlation of the i-element.

The measured total relative phase ϕ_{ij} is, in first approximation, the sum of two terms:

$$\phi_{ij} = \varphi_{ij} + \omega\tau_g \quad (5)$$

Where φ_{ij} is the unknown relative instrumental phase (due to cables, receivers, electronics, etc.) of the i-element with respect to the j-element, $\omega = 2\pi v$ is the pulsation of the incoming signal and τ_g is the geometric delay. The latter term can be calculated from the hexacopter position at a given time, provided by the differential GNSS/GPS system, and the antenna coordinates as:

$$\tau_g = \frac{r_j - r_i}{c} \quad (6)$$

In which r_i and r_j are the distance from the given elements to the hexacopter and *c* is the light speed.

Finally the phase correction that have to be applied to the j-element, taking the i-element as phase reference, will be:

$$\varphi_j = \varphi_i - \varphi_{ij} = -atan2\left(\frac{Imag(R_{ij})}{\sqrt{R_{ii}R_{jj}}}, \frac{Real(R_{ij})}{\sqrt{R_{ii}R_{jj}}}\right) + \omega\tau_g \quad (7)$$

In practice each correction coefficient is calculated from the average of a number of correlator samples.

The phase correction coefficients for each antenna were calculated as in Table 5.

Element ID	Phase correction	Element ID	Phase correction
V001	$\varphi_{(V007\_V001)}$	**H001**	$-\varphi_{(H001\_H009)}$
V002	$\varphi_{(V007\_V002)}$	**H002**	$\varphi_{(H009\_H002)}$
V003	$-\varphi_{(V003\_V007)}$	**H003**	$\varphi_{(H009\_H003)}$
V004	$-\varphi_{(V003\_V007)} + \varphi_{(V003\_V004)}$	**H004**	$\varphi_{(H009\_H004)}$
V005	$\varphi_{(V007\_V005)}$	**H005**	$\varphi_{(H009\_H005)}$
V006	$\varphi_{(V007\_V006)}$	**H006**	$-\varphi_{(H001\_H009)} + \varphi_{(H001\_H006)}$
V007	0	**H007**	$\varphi_{(H009\_H007)}$
V008	$-\varphi_{(V003\_V007)} + \varphi_{(V003\_V008)}$	**H008**	$-\varphi_{(H001\_H009)} + \varphi_{(H001\_H008)}$
V009	$\varphi_{(V007\_V009)}$	**H009**	0

Table 5 - Calculation of the phase correction coefficients from the relative phases of the selected baselines.

The good repeatability of the phase measurements as well as the phase stability of the receiving chains can be verified by the comparison between the phase calibration coefficients calculated in different times (flights), as shown in Table 6. Some discrepancies in the phase measurements could be reduced, as instance,

including the hexacopter asset angles in the calibration algorithm (here were not considered) as well increasing the sampling rate of the hexacopter position, that in MAD-3 was 1 Hz.

Antenna ID	Flight 134_1		Flight 134_3		Flight 142_1		Flight 541_1	
	ϕ	σ_ϕ	ϕ	σ_ϕ	ϕ	σ_ϕ	ϕ	σ_ϕ
V001	83.2	0.9	83.5	0.5	86.6	2.3	80.8	1.1
V002	132.8	0.6	130.0	0.5	134.3	2.2	133.9	1.2
V003	126.6	0.7	123.7	0.5	126.2	2.5	127.2	1.7
V004	267.1	1.5	264.8	1.1	265.7	4.3	266.4	3.1
V005	1.71	0.6	358.7	0.4	12.5	1.4	9.7	0.9
V006	196.7	1.1	193.3	0.5	197.8	2.1	201.8	1.5
V007	0	0	0	0	0	0	0	0
V008	346.7	1.5	344.2	1.1	346.3	4.7	352.3	3.1
V009	323.5	1.1	320.4	0.8	318.7	2.2	329.7	1.4

Table 6 – Phase calibration coefficients ϕ and their standard deviations σ_ϕ (in deg) calculated in different flights for the V-pol.

Fig. 16 shows the fringes of the 8 baselines before the calibration (in which phase correction coefficients were set to zero) obtained in the V-Polarization with a hexacopter NS trajectory. The fringes are normalized to unity at their maximum absolute value.

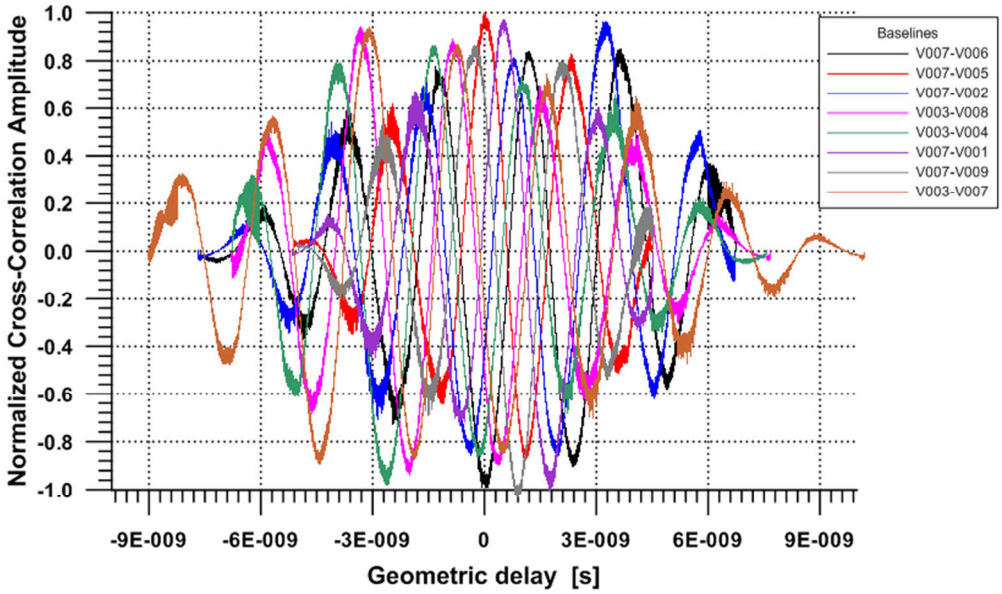

Fig. 16 - (Flight 142_5) Normalized fringe patterns (V-Pol) before phase calibration.

The fringe patterns after the phase calibration performed by means the coefficients calculated in the stationary flight are plotted in Fig. 17.

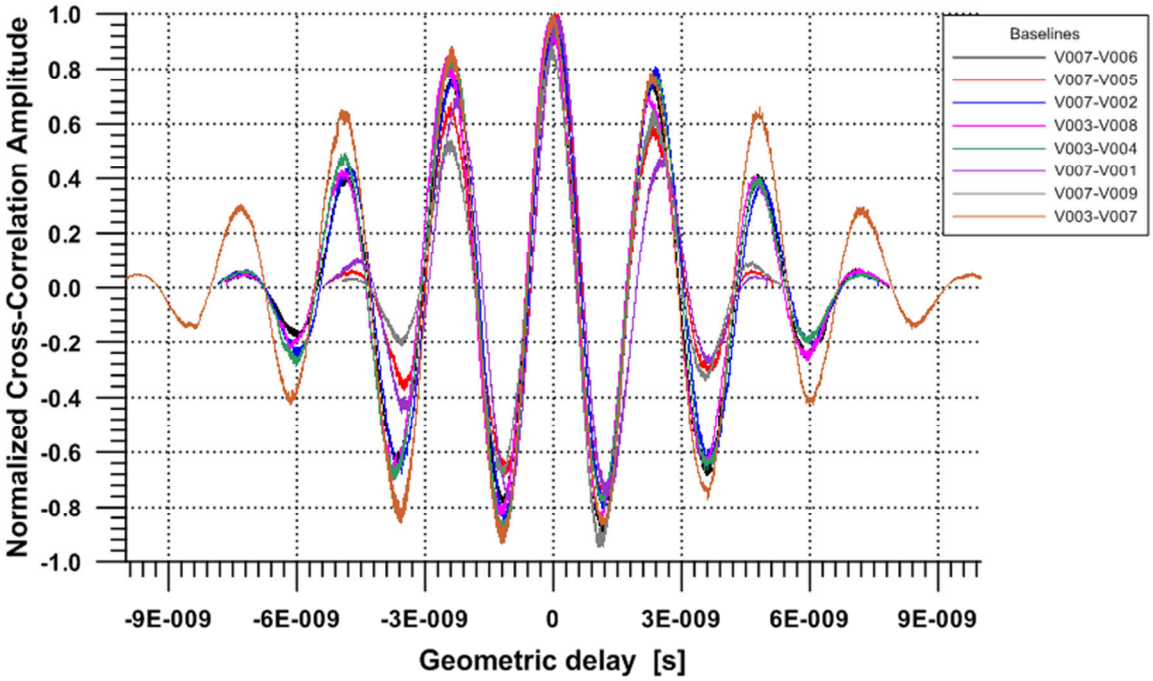

Fig. 17 – (Flight 331_1) Normalized fringe patterns (V-Pol) after phase calibration.

Although all the main fringe maxima are almost correctly aligned at zenith (geometric delay = 0 s), that was the position of the hexacopter in the calibration flight, various secondary maxima exhibit noticeable x-axis offsets depending on the baseline. These offsets are mainly due to the phase antenna pattern, that is a direction dependent effect. This has been confirmed from the comparison between the observed fringes and the simulated ones with and without phase pattern corrections. Fig. 18 displays the observed fringe pattern of the V007-V001 baseline compared with simulations. Both simulations have been aligned with the main maximum of the observed fringe pattern that is not perfectly aligned to the zero of geometric delay, because of the limited accuracy of the measurements used for the phase calibration. There is a very good agreement between the corrected simulation (red curve) and the positions of the observed fringe maxima. The differences in the fringe amplitudes between simulation and measurement, evident at positive geometric delays (right part of Fig. 18), are probably caused by the ideal hexacopter path considered in these preliminary simulations.

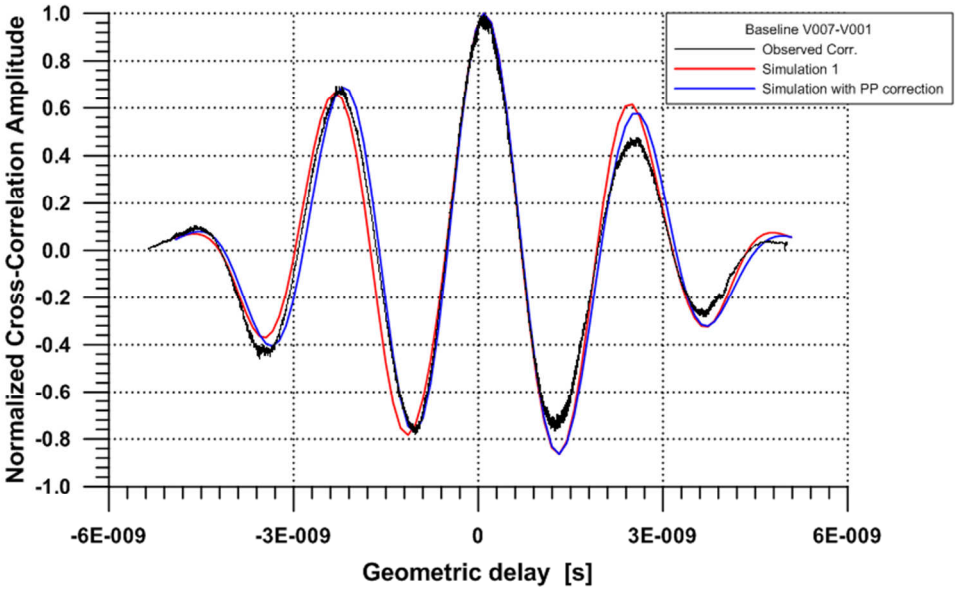

Fig. 18 – (Flight 331_1) Measured fringe pattern of V007-V001 baseline (black line) and its simulation without (red line) and with (blue line) phase pattern corrections.

Therefore the measured phase equation has to be modified as follow:

$$\phi_{ij}(\theta,\varphi) = \varphi_{ij}(\theta,\varphi) + \omega\tau_g + \Delta\phi_{ij}(\theta,\varphi) \qquad (8)$$

Where $\Delta\phi_{ij}(\theta,\varphi)$ is the additive phase pattern term due to the mutual coupling between the array elements and to the intrinsic antenna phase patterns.

MAD-3 campaign allowed also to measure directly this phase pattern. In fact, when the array has been already calibrated at zenith by means the phase corrections calculated by Eq. 7, the residual phase error for each baseline is exactly the phase pattern along the hexacopter trajectory for that baseline. A comparison between observed and simulated phase patterns has been performed. Even if these preliminary simulations have been calculated along an ideal trajectory (E-plane) and without hexacopter asset angles corrections, the trend of the observed and simulated phase patterns are in good agreement (Fig. 19).

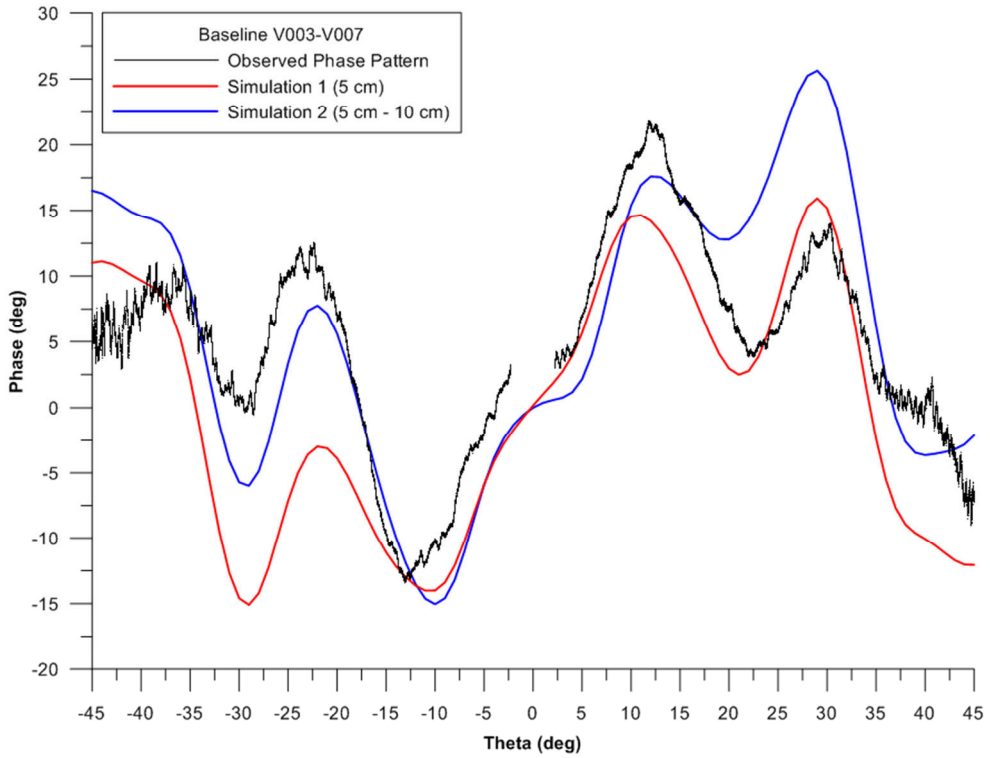

Fig. 19 – Comparison between the measured phase pattern obtained for the baseline V003-V007 (black line) and simulations considering a ground distance of 5 cm for both elements (red line) or 5 cm for V003 and 10 cm for V007 (blue line).

7.4 Array patterns

Fig. 20 shows the E-plane and H-plane array patterns for different flights.

The same electromagnetic model used for simulating the embedded-element patterns shown in the previous section has been used also to compute the array pattern.

Two sets of weights for each antenna of the array have been used: *(i)* the first has been obtained equalizing the amplitudes of all the element patterns at the zenith and *(ii)* the second has been obtained equalizing also the phases at the zenith.

As a matter of fact, it should be noted that all the embedded-element patterns are slightly different to each other in terms of both amplitude and phase, owing to their different position in the array and their different distance from the ground. As evident from Fig. 18, the second method provides results which better agree with the experimental measurements.

The system shows a good dynamic range and the overall agreement is good. There are some discrepancies in the secondary lobes and some occasional offsets, but they are highly dependent on both modeling and calibration inaccuracy.

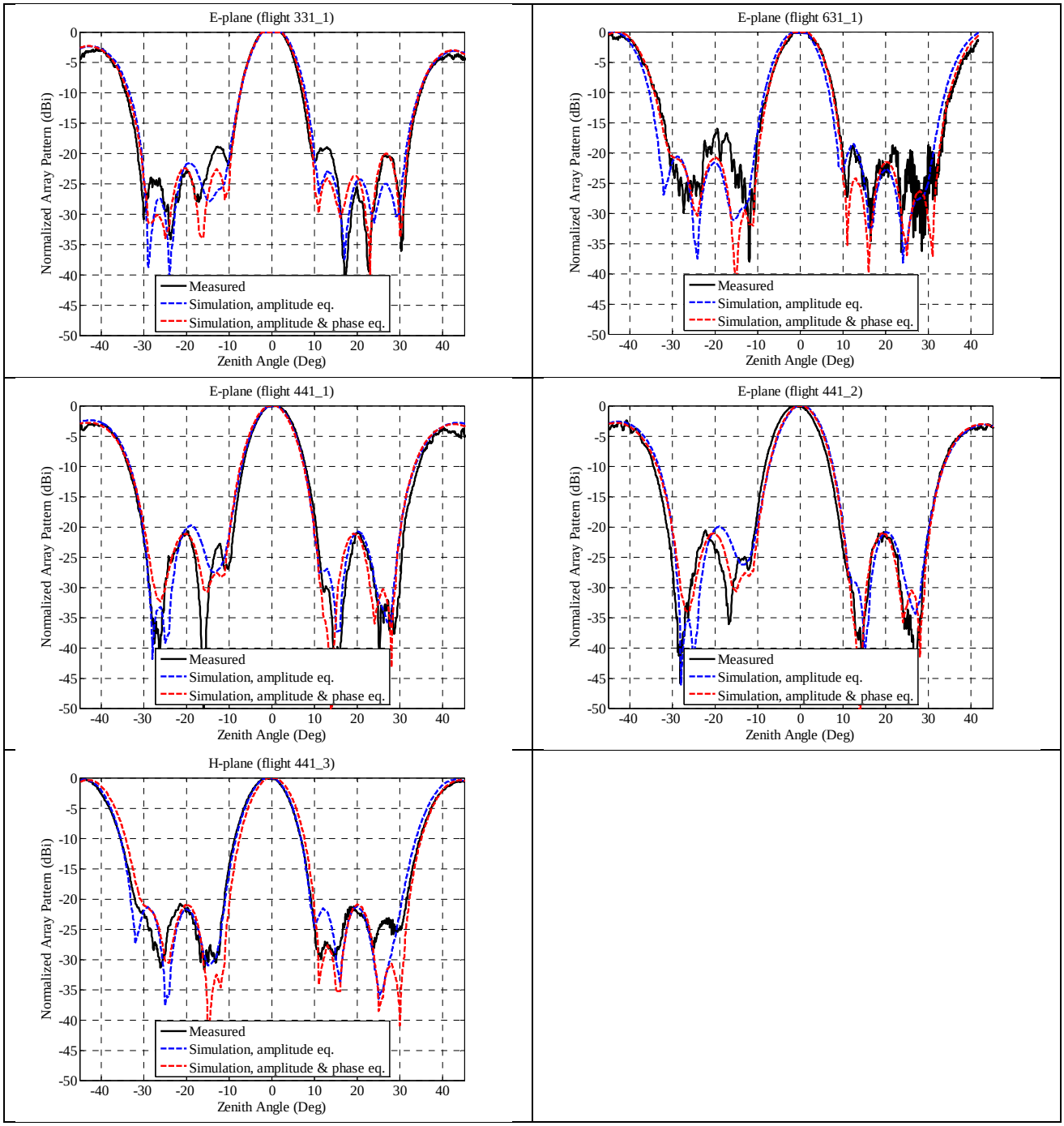

Fig. 20 - E-plane array pattern compared to simulations (flight 331_1, flight 631_1, flight 441_1, flight 441_2); H-plane array pattern compared to simulations (flight 441_3).

7.5 Residual phase errors

The phase calibration of the array is performed with the UAV close to zenith. In particular, the zenith position is set as a goal for the navigation system. Actually, the real UAV position can generally be 2 or 3 meters far from such a goal. Nevertheless, such a discrepancy is compensated for (only for the geometrical delay), using the accurate position information measured by the differential GNSS system.

Several tests on this calibration condition have been performed from 22nd to 23rd of May 2014. The best and worst results are discussed in this section and compared to the expected performances.

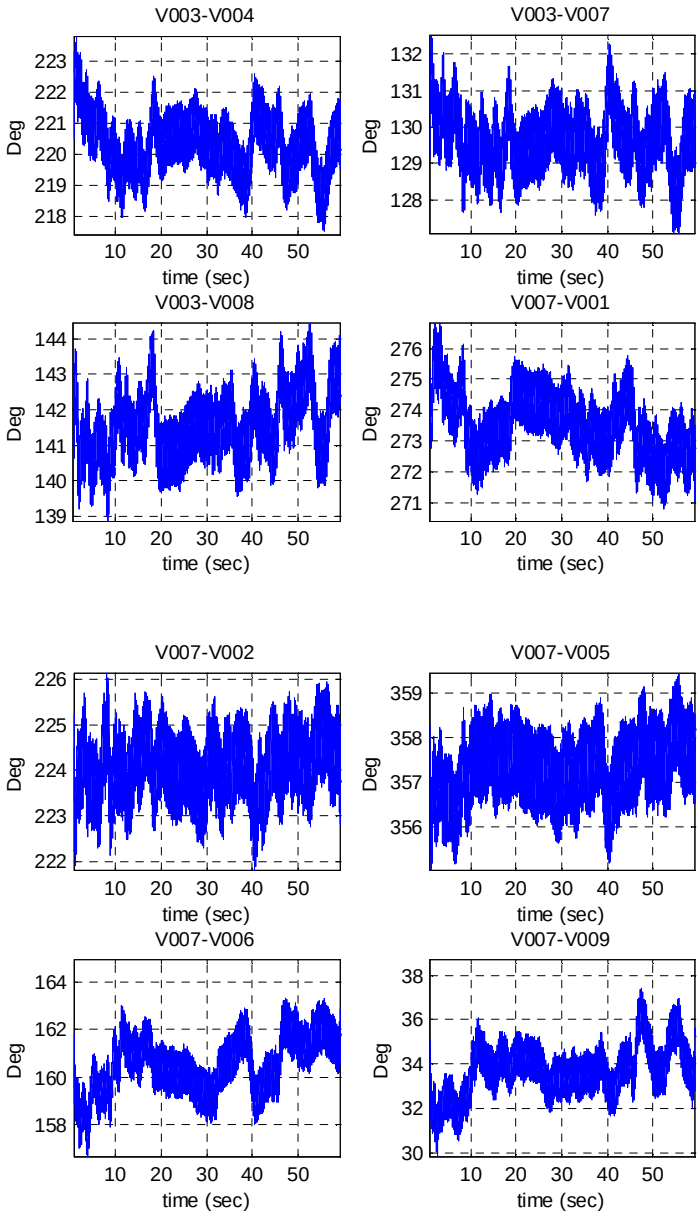

Fig. 21 – (Flight 134_1) UAV position is set to zenith. Compensated phase differences measured at the eight baselines of the MAD array.

Fig. 21 shows the phase difference measured at the eight baselines of MAD-3 during a 60-sec snapshot of the flight 134_1 on the 22nd of May 2014. All the phases are stable within about ± 2 Deg. This residual error is mainly related to two different factors: the phase noise produced by the quantization errors of the back-end and the accuracy of the differential GNSS system. An estimation of the latter is given by the differential GNSS elaboration software in terms of standard deviation for each measured point. The obtained data for flight 134_1 are reported in Fig. 22. The x and y coordinates show a distance from zenith which ranges from 1 to -2.5 m whereas the z coordinate shows a flying height of about 100 m. The standard deviations are below 2 cm for both the x and y coordinates, and below 5 cm for the z one. It should be pointed out that these values are in perfect agreement to the expected performances of a differential GNSS measurement system.

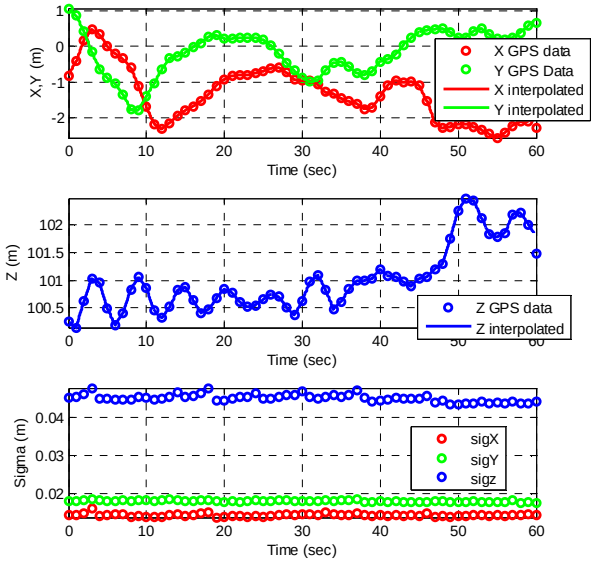

Fig. 22 - Measured UAV position during the flight n. 134_1 and estimated standard deviations.

The effect of the GNSS accuracy on the residual phase error can be evaluated with simple considerations. Let us limit the discussion on a baseline which is completely oriented along the y axis (like the V7-V3 of the MAD Array). An UAV position error Δ_y will produce a corresponding error in the observation angle

$$\Delta\vartheta = \tan^{-1}\frac{\Delta_y}{z}$$

where z is the flying height of the UAV. According to the far-field approximation, the error $\Delta\vartheta$ will produce a differential phase error $\Delta\varphi$ between the two received signals at the considered baseline, which can be expressed as

$$\Delta\varphi = \frac{2\pi}{\lambda} L_{baseline} \sin\Delta\vartheta$$

where $L_{baseline}$ is the distance between the two antennas. By linearization, the following relationship between the standard deviation of position measurements and the standard deviation of the differential phase can be written

$$\sigma_\varphi \cong \frac{2\pi}{\lambda} L_{baseline} \frac{\sigma_y}{z}$$

Fig. 23 shows the standard deviations for baseline V7-V3. The obtained value for σ_φ is less than 0.4 Deg.

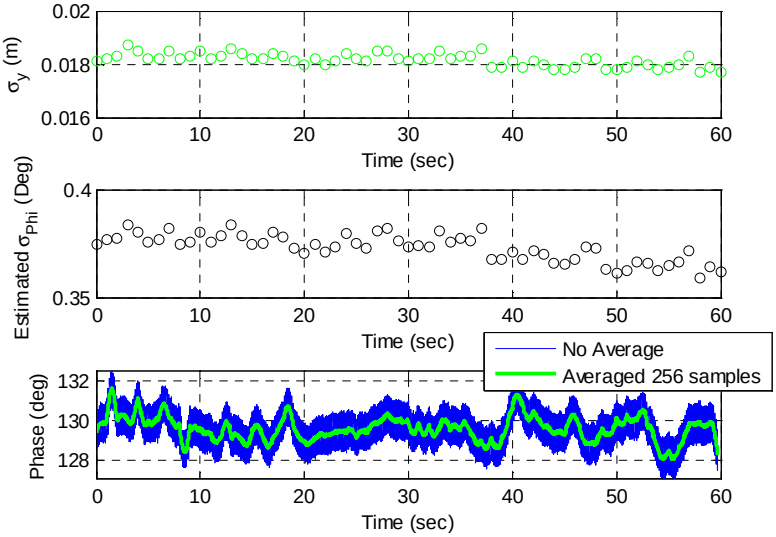

Fig. 23 – (Flight 134_1) Standard deviation of the y coordinate (green circles) and estimated standard deviation of the differential phase (black circles). Measured differential phase at baseline V7-V3: no averaging (blue), 256-sample average (green solid line).

Fig. 23 also reports the measured phase for baseline V7-V3 (blue line). Moreover, that the phase noise due to the quantization errors in the back-end has been averaged out obtaining the green solid curve.

The same averaged curve is reported in Fig. 24. The red error bars have been obtained as $\mu \pm \sigma_\varphi$, where μ is the average value of the trace on the 60-sec snapshot. The measured standard deviation $\tilde{\sigma}_\varphi$ has also been estimated from the trace (0.6 Deg). The black error bars are hence $\mu \pm \tilde{\sigma}_\varphi$. The two standard deviations are quite close to each other confirming the consistency of the overall measurement system.

It should be noted that the phase peaks in Fig. 24 mainly occur in the intervals between two adjacent seconds. This phenomenon is related to the interpolation error of GNSS position data. The latter are in fact given with a sample rate of 1 Hz, whereas the sample rate of the RF data is much higher. In order to filter out this interpolation error, the green curve in Fig. 24 has been sampled at 1 Hz as well. In other words, the number of phase samples has been decimated to meet the same sampling rate of the position data. The resulting curve is the blue one in Fig. 25, showing a smoother behavior with respect to the green curve in Fig. 24. A new standard deviation $\hat{\sigma}_\varphi$ has been computed (0.55 Deg) obtaining a slightly lower value with respect to $\tilde{\sigma}_\varphi$.

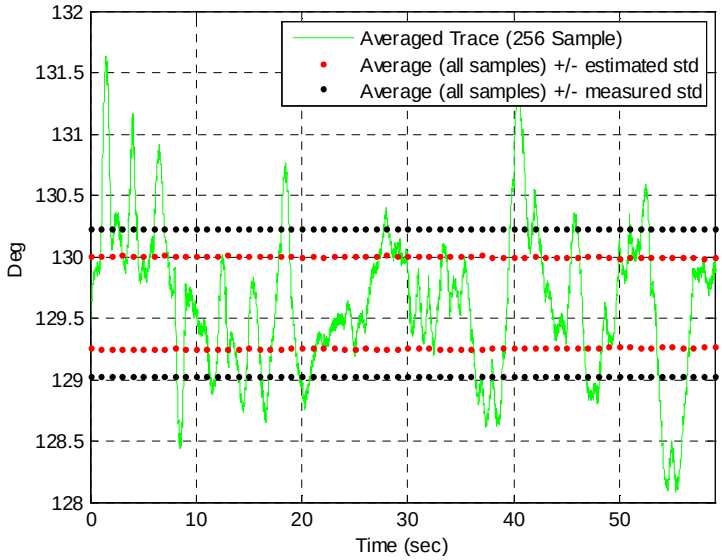

Fig. 24 - (Flight 134_1) Averaged phase difference for baseline V7-V3 with estimated (red dots) and measured (black dots) standard deviations.

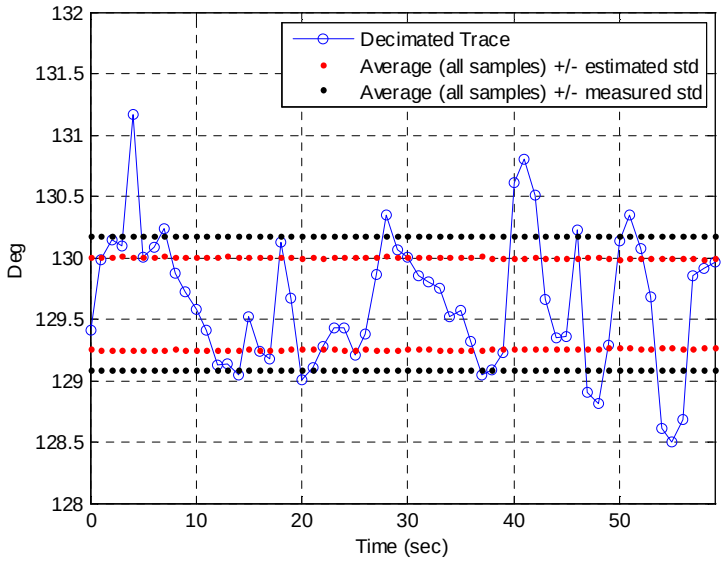

Fig. 25 - (Flight 134_1) Decimated phase difference for baseline V7-V3 with estimated (red dots) and measured (black dots) standard deviations.

The obtained standard deviations for baseline V7-V3 are reported in Table 7. The additional column shows the corresponding data obtained for baseline V7-V5. The halved distance between the antennas leads to a halved estimated standard deviation (0.2 Deg) with respect to baseline V7-V3. The measured standard deviation is instead just reduced of about 25%. In other words, the discrepancy of about 0.2 Deg between estimated and measured standard deviations is preserved for the shorter baselines as well. It means that

this small error is not related to the position error of the differential GNSS system, whose effect is instead proportional to $L_{baseline}$.

	Unit	Baseline V7-V3	Baseline V7-V5
Distance between antennas	m	4.24	2.21
Estimated STD	Deg	0.374	0.187
Measured STD of averaged trace (256 samples)	Deg	0.601	0.439
Measured STD on the decimated trace (one sample per second)	Deg	0.547	0.421

Table 7 - (Flight 134_1) Estimated and measured standard deviations for baselines V7-V3 and V7-V5.

A similar analysis has been carried out also for a second flight. The position data for flight 142_1 are reported in Fig. 26. The x and y coordinates are about 1 m apart from zenith, the z coordinate show a flying height slightly lower than 100 m. The standard deviations of the hexacopter positions are really good (see bottom panel of Fig. 26). They produce an estimated phase error σ_φ of about 0.35 Deg, visible in Fig. 27. However, the observed phase variation is about ± 5 Deg.

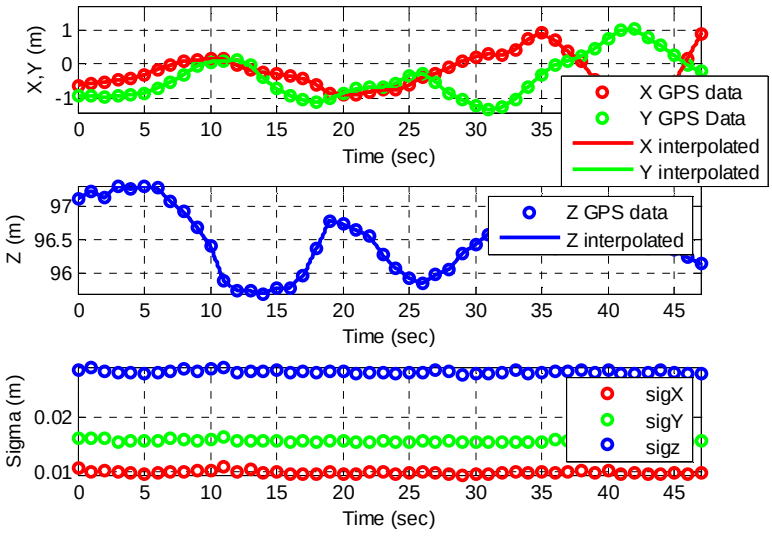

Fig. 26 - Measured UAV position during the flight n. 142_1 and estimated standard deviations.

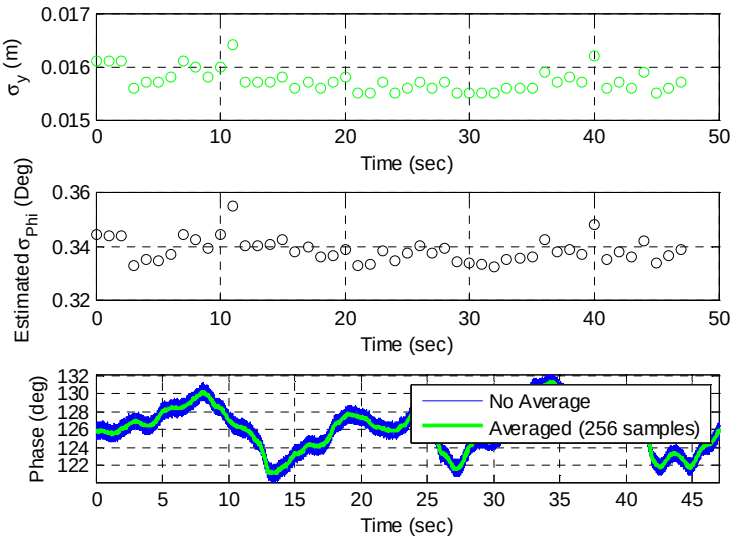

Fig. 27 – (Flight 142_1) Standard deviation of the y coordinate (green circles) and estimated standard deviation of the differential phase (black circles). Measured differential phase at baseline V7-V3: no averaging (blue), 256-sample average (green solid line).

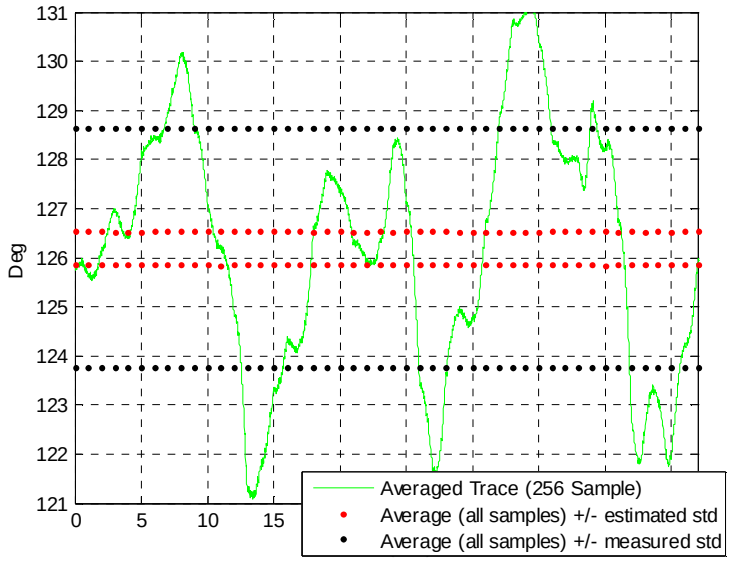

Fig. 28 - (Flight 142_1) Averaged phase difference for baseline V7-V3 with estimated (red dots) and measured (black dots) standard deviations.

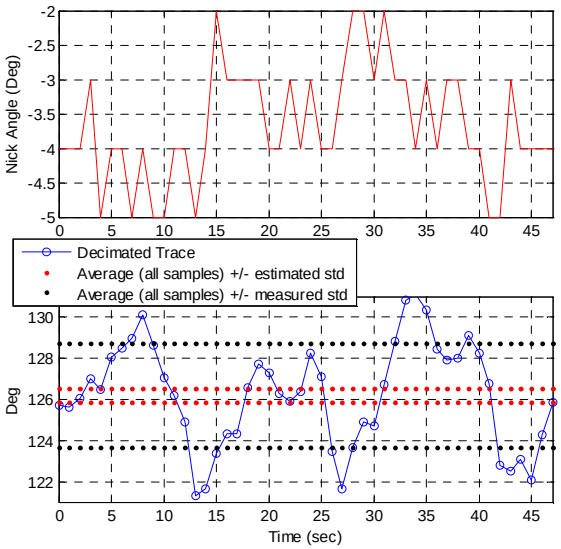

Fig. 29 - (Flight 142_1) Nick angle measured by the UAV (top). Decimated phase difference for baseline V7-V3 with estimated (red dots) and measured (black dots) standard deviations (bottom).

The same variation is also visible in the averaged and decimated curves reported in Fig. 28 and Fig. 29, respectively. The measured standard deviations $\tilde{\sigma}_{\varphi}$ and $\hat{\sigma}_{\varphi}$ are about 2.5 Deg i.e. about four times larger than the one obtained with flight 134_1. A subsequent flight on the 23rd of May showed a similar behavior as well.

It should be pointed out that there was a lot of wind on the 23rd of May. Whereas almost no wind was present on the 22nd of May (Flight 134_1).

The nick angle is also shown in Fig. 29 in order to find some possible correlation with the residual phase error. However, the relationship between the two curves does not become apparent.

	Unit	Baseline V7-V3	Baseline V7-V5
Distance between antennas	m	4.24	2.21
Estimated STD	Deg	0.339	0.169
Measured STD of averaged trace (256 samples)	Deg	2.44	1.348
Measured STD on the decimated trace (one sample per second)	Deg	2.52	1.394

Table 8 - (Flight 142_1) Estimated and measured standard deviations for baselines V7-V3 and V7-V5.

As reported in the last column of Table 8, the measured standard deviations for the baseline V7-V5 are almost halved with respect to the ones in the V7-V3 column. This fact demonstrate that the increased standard deviation is consistent with an increased error on the GNSS measured data, probably related to the presence of wind producing significant oscillations of the UAV.

8. Lessons learned from MAD-3 and conclusions and future works

The measurement session of MAD-3 can be considered successfully performed. The experimental embedded antenna and array beam patterns agree very well with the numerical results and they show also repeatability. Some problems coming from MAD-2 have been solved and the results now agree better thanks for example to the correction for the angles of the hexacopter. The new session also explains the residual phase errors, even if not completely.

As far as the hexacopter system, the differential GNSS/GPS tracking system has worked correctly and the photogrammetry has been consolidated as optimal solution for measuring the antennas positions; the main problems have been:

- Data-link failures due to soldering issues in the telemetry transmitter on board of the hexacopter;
- broken pin in the SSD connector of ground GNSS receiver.

MAD-3 campaign has represented a significant improvement also from the back-end and array calibration point of view. In particular, concerning the back-end:

- the automatic analogue equalization system was successfully tested;
- a new back-end firmware was implemented with following advantages:
  - Flexibility due to a fully programmable baseline set.
  - Capability to simultaneously acquire both polarizations.
  - Reduction of the network infrastructure because data from correlator and beamformer are encapsulated in the same data packet.
  - Capability to acquire the Full Correlation Matrix

In MAD-3 the “snapshot” calibration procedure was successfully tested. It has better performances respect to the “fringe fitting” technique adopted in the previous MAD campaigns, because the “fringe fitting” method assumes there is no contribution of the phase pattern, but it was demonstrated that the phase pattern influence is not negligible. This direction dependent effect reduces the “fringe fitting” method accuracy and its applicability only to a limited types of trajectories/directions. On the contrary, the “snapshot” method does not suffer of this restriction and it is able to:

- calibrate the system in the desired direction;
- measure the phase pattern along the hexacopter trajectory.

The calibration procedure accuracy could be further improved including additional information, as the hexacopter orientation angles, in the algorithm.

The improvement activity on the UAV test source in terms of optimum routing of the cables on the hexacopter arms, proper RF grounding of the arms and improved balun section produced a better agreement between measurement and simulations. The software correction for hexacopter orientation angles allowed for a good amplitude-pattern accuracy also during severe wind conditions. The flying height of 100 m instead of 70 m produce lower errors on measured observation angles of the test source. This choice allows one to compensate for the slightly higher position errors of the differential GNSS system with respect to the total station (MAD-2).

As a future work, we plan to perform:

- array cross-polarization measurement;
- different, smart, calibration procedures;
- array measurements with calibration phase evaluated for different antenna pointing (than zenith).
- a new package is being developed for the balun section, in order to further improve the performance of the test source in terms of symmetry of the pattern and cross-pol level.
- further error analysis is required to understand the phase ripple obtained in high wind conditions.
- The agreement between measurement and simulations for both amplitude and phase data demonstrates that the new calibration procedures can be carefully studied in advance with simulations.
- create a complete data elaboration/visualization tool for the MAD-3 back-end. This will speed-up the overall measurement campaign.
- further improvement of the back-end firmware (e.g. to avoid data packet loss).
- IXR measurement.
- instantaneous wideband measurement.
- larger array calibration / characterization.
- astronomical observation of strong radio sources.

Further investigations on different baselines definitions will be considered to eventually optimize the antenna characterization also in different planes or possibly assuring an uniform coverage.

Acknowledgments

We are grateful to Stefan Wijnholds and to all Medicina technical staff for their important support to the MAD-3 campaign. We wish to thanks also Kristian Zarb Adami, Jack Hickish, Griffin Foster and Alessio Magro for the digital backend setup.

List of abbreviations

ADC = Analog to Digital Converter

AAVS = Aperture Array Verification System

AAVP = Aperture Array Verification Programme

BEST-2 = Basic Element for SKA Training 2

CST = Computer Simulation Technology ®

CW = Continuous Wave

FE = Front-End

FFT = Fast Fourier Transform

FPGA = Field Programmable Gate Array

GbE = Gigabit Ethernet

GNSS = Global Navigation Satellite System

GPS = Global Positioning System

IF = Intermediate Frequency

IXR = Intrinsic Cross-Polarization Ratio

LFAA = Low Frequency Aperture Array

LNA = Low Noise Amplifier

MAD = Medicina Array Demonstrator

NTP = Network Time Protocol

ORX = Optical Receiver

OTX = Optical Transmitter

PFB = Polyphase Filter Bank

PPS = Pulse per Second

RF = Radio Frequency

RX = Receiver

ROACH = Reconfigurable Open Architecture Computing Hardware

SKA = Square Kilometre Array

TX = Transmitter

UAV = Unmanned Aerial Vehicle

References

[1] https://www.skatelescope.org/home/technicaldatainfo/key-documents/

[2] G. Pupillo, G. Naldi, A. Mattana, J. Monari, F. Perini, M. Schiaffino, P. Bolli, G. Virone, A. Lingua, "The 2nd Measurement Campaign of the Medicina Array Demonstrator", Technical Report, INAF-IRA 479/14.

[3] G. Virone et al., "UAV-based Radiation Pattern Verification for a Small Low-Frequency Array," IEEE International Symposium on Antennas and Propagation and USNC-URSI National Radio Science Meeting 2014, July 6-12 2014, Memphis, Tennessee, USA.

[4] A. Lingua, I. Aicardi, H. Bendea, P. Maschio, M. Piras, "Operazioni geomatiche rivolte all'utilizzo di droni per la caratterizzazione di antenne per radioastronomia", Report n. 3_2014, Politecnico di Torino, Giugno 2014.

[5] F. Perini, M. Schiaffino, S. Mariotti J. Monari "INAF/IRA AAlo AAVS0 LNA", Technical Report, INAF-IRA 463/12.

[6] F. Perini, "ANALOGUE OPTICAL LINKS EXPERIENCES IN THE FRAMEWORK OF THE SKA/BEST ACTIVITIES", Wide Field Science and Technology for the Square Kilometre Array, Proceedings of the SKADS Conference held at the Chateau de Limelette, Belgium, 3-6 November 2009. http://pos.sissa.it/archive/conferences/132/061/SKADS%202009_061.pdf

[7] F. Perini, G. Bianchi, M. Schiaffino, J. Monari, "BEST RECEIVER EXPERIENCE: GENERAL ARCHITECTURE, DESIGN AND INTEGRATION", Wide Field Science and Technology for the Square Kilometre Array, Proceedings of the SKADS Conference held at the Chateau de Limelette, Belgium, 3-6 November 2009. http://pos.sissa.it/archive/conferences/132/062/SKADS%202009_062.pdf

[8] G. Virone, et al. "Broadband array element for the SKA low-frequency aperture array", International Conference on Electromagnetics in Advanced Applications (ICEAA), 12-16 September 2011.

[9] J. Monari, et al. "Aperture Array for Low Frequency: the Vivaldi solution", International Conference on Electromagnetics in Advanced Applications (ICEAA), Turin, 9-13 September 2013.

[10] G. Virone, et al., "Antenna Pattern Verification System Based on a Micro Unmanned Aerial Vehicle (UAV)", IEEE ANTENNAS AND WIRELESS PROPAGATION LETTERS, vol. 13, 2014.

[11] A. C. Ludwig, "The definition of cross polarization," IEEE Transaction on Antennas and Propagation, vol. 21, pp. 116-119, Jan 1973.